The Astronomical Journal, 163:168 (18pp), 2022 April https://doi.org/10.3847/1538-3881/ac50a9

A Second Planet Transiting LTT 1445A and a Determination of the Masses of Both Worlds

Jennifer G. Winters[1], Ryan Cloutier[1,61], Amber A. Medina[1], Jonathan M. Irwin[1], David Charbonneau[1], Nicola Astudillo-Defru[2], Xavier Bonfils[3], Andrew W. Howard[4], Howard Isaacson[5,6], Jacob L. Bean[7], Andreas Seifahrt[7], Johanna K. Teske[8], Jason D. Eastman[1], Joseph D. Twicken[9,10], Karen A. Collins[1], Eric L. N. Jensen[11], Samuel N. Quinn[1], Matthew J. Payne[1], Martti H. Kristiansen[12,13], Alton Spencer[14], Andrew Vanderburg[15], Mathias Zechmeister[16], Lauren M. Weiss[17], Sharon Xuesong Wang[18], Gavin Wang[19,20], Stéphane Udry[21], Ivan A. Terentev[22], Julian Stürmer[23], Gudmundur Stefánsson[24,64], Avi Shporer[15], Stephen Shectman[25], Ramotholo Sefako[26], Hans Martin Schwengeler[27], Richard P. Schwarz[28], Nicholas Scarsdale[29], Ryan A. Rubenzahl[4,62], Arpita Roy[30,31], Lee J. Rosenthal[4], Paul Robertson[32], Erik A. Petigura[33], Francesco Pepe[21], Mark Omohundro[34], Joseph M. Akana Murphy[35,62], Felipe Murgas[36,37], Teo Močnik[38], Benjamin T. Montet[39,40], Ronald Mennickent[41], Andrew W. Mayo[42,43], Bob Massey[44], Jack Lubin[32], Christophe Lovis[21], Pablo Lewin[45], David Kasper[7], Stephen R. Kane[46], Jon M. Jenkins[10], Daniel Huber[47], Keith Horne[48], Michelle L. Hill[46], Paula Gorrini[16], Steven Giacalone[42], Benjamin Fulton[49], Thierry Forveille[3], Pedro Figueira[50,51], Tara Fetherolf[52,65], Courtney Dressing[5], Rodrigo F. Díaz[53], Xavier Delfosse[3], Paul A. Dalba[35,46,63], Fei Dai[54], C. C. Cortés[41,55], Ian J. M. Crossfield[56], Jeffrey D. Crane[25], Dennis M. Conti[57], Kevin I. Collins[58], Ashley Chontos[47,62], R. Paul Butler[59], Peyton Brown[60], Madison Brady[7], Aida Behmard[54,62], Corey Beard[32], Natalie M. Batalha[29], and Jose-Manuel Almenara[3]

[1] Center for Astrophysics | Harvard & Smithsonian, 60 Garden Street, Cambridge, MA 02138, USA; jennifer.winters@cfa.harvard.edu
[2] Departamento de Matemática y Física Aplicadas, Universidad Católica de la Santísima Concepción, Alonso de Rivera 2850, Concepción, Chile
[3] Université Grenoble Alpes, CNRS, IPAG, F-38000 Grenoble, France
[4] Department of Astronomy, California Institute of Technology, Pasadena, CA 91125, USA
[5] Department of Astronomy, University of California Berkeley, Berkeley, CA 94720, USA
[6] Centre for Astrophysics, University of Southern Queensland, Toowoomba, QLD, Australia
[7] Department of Astronomy & Astrophysics, University of Chicago, 5640 S. Ellis Avenue, Chicago, IL 60637, USA
[8] Earth & Planets Laboratory of the Carnegie Institution for Science, 5241 Broad Branch Road, NW, Washington, DC 20015, USA
[9] SETI Institute, Moffett Field, CA 94035, USA
[10] NASA Ames Research Center, Moffett Field, CA 94035, USA
[11] Department of Physics & Astronomy, Swarthmore College, Swarthmore, PA 19081, USA
[12] Brorfelde Observatory, Observator Gyldenkernes Vej 7, DK-4340 Tølløse, Denmark
[13] DTU Space, National Space Institute, Technical University of Denmark, Elektrovej 327, DK-2800 Lyngby, Denmark
[14] Western Connecticut State University, Danbury, CT 06810, USA
[15] Department of Physics and Kavli Institute for Astrophysics and Space Research, Massachusetts Institute of Technology, Cambridge, MA 02139, USA
[16] Institut für Astrophysik, Georg-August-Universität, Friedrich- Hund-Platz 1, D-37077 Göttingen, Germany
[17] Department of Physics, University of Notre Dame, Nieuwland Science Hall, Notre Dame, IN 46556, USA
[18] Department of Astronomy, Tsinghua University, Beijing 100084, People's Republic of China
[19] Tsinghua International School, Beijing 100084, People's Republic of China
[20] Stanford Online High School, 415 Broadway Academy Hall, Floor 2, 8853, Redwood City, CA 94063, USA
[21] Observatoire de Genève, Université de Genève, Chemin Pegasi 51, 1290 Sauverny, Switzerland
[22] Citizen Scientist, Planet Hunter, Petrozavodsk, Russia
[23] Landessternwarte, Zentrum für Astronomie der Universität Heidelberg, Königstuhl 12, D-69117 Heidelberg, Germany
[24] Princeton University, Department of Astrophysical Sciences, 4 Ivy Lane, Princeton, NJ 08540, USA
[25] The Observatories of the Carnegie Institution for Science, 813 Santa Barbara Street, Pasadena, CA 91101, USA
[26] South African Astronomical Observatory, P.O. Box 9, Observatory, Cape Town 7935, South Africa
[27] Citizen Scientist, Planet Hunter, Bottmingen, Switzerland
[28] Patashnick Voorheesville Observatory, Voorheesville, NY 12186, USA
[29] Department of Astronomy and Astrophysics, University of California, Santa Cruz, CA 95060, USA
[30] Space Telescope Science Institute, 3700 San Martin Drive, Baltimore, MD 21218, USA
[31] Department of Physics and Astronomy, Johns Hopkins University, 3400 N Charles Street, Baltimore, MD 21218, USA
[32] Department of Physics & Astronomy, University of California Irvine, Irvine, CA 92697, USA
[33] Department of Physics & Astronomy, University of California Los Angeles, Los Angeles, CA 90095, USA
[34] Citizen Scientist, c/o Zooniverse, Department of Physics, University of Oxford, Denys Wilkinson Building, Keble Road, Oxford, OX1 3RH, UK
[35] Department of Astronomy and Astrophysics, University of California, Santa Cruz, CA 95064, USA
[36] Instituo de Astrofísica da Canarias (IAC), E-38205 La Laguna, Tenerife, Spain
[37] Departamento de Astrofísica, Universidad de La Laguna (ULL), E-38206 La Laguna, Tenerife, Spain
[38] Gemini Observatory/NSF's NOIRLab, 670 N. A'ohoku Place, Hilo, HI 96720, USA
[39] School of Physics, University of New South Wales, Sydney, NSW 2052, Australia
[40] UNSW Data Science Hub, University of New South Wales, Sydney, NSW 2052, Australia
[41] Departamento de Astronomía, Universidad de Concepción, Casilla 160-C, Concepción, Chile
[42] Department of Astronomy, University of California Berkeley, Berkeley, CA 94720, USA
[43] Centre for Star and Planet Formation, Natural History Museum of Denmark & Niels Bohr Institute, University of Copenhagen, Øster Voldgade 5-7, DK-1350 Copenhagen K., Denmark
[44] Villa '39 Observatory, Landers, CA 92285, USA
[45] The Maury Lewin Astronomical Observatory, Glendora, CA 91741, USA
[46] Department of Earth and Planetary Sciences, University of California, Riverside, CA 92521, USA
[47] Institute for Astronomy, University of Hawai'i, 2680 Woodlawn Drive, Honolulu, HI 96822, USA

[48] SUPA Physics and Astronomy, University of St. Andrews, Fife, KY16 9SS, UK
[49] NASA Exoplanet Science Institute/Caltech-IPAC, MC 314-6, 1200 E. California Boulevard, Pasadena, CA 91125, USA
[50] European Southern Observatory, Alonso de Córdova 3107, Vitacura, Región Metropolitana, Chile
[51] Instituto de Astrofísica e Ciências do Espaço, Universidade do Porto, CAUP, Rua das Estrelas, 4150-762 Porto, Portugal
[52] Earth and Planetary Sciences Department, University of California, Riverside, CA 92521, USA
[53] International Center for Advanced Studies (ICAS) and ICIFI (CONICET), ECyT-UNSAM, Campus Miguelete, 25 de Mayo y Francia, (1650) Buenos Aires, Argentina
[54] Division of Geological and Planetary Sciences, California Institute of Technology, Pasadena, CA 91125, USA
[55] Departamento de Física, Facultad de Ciencias, Universidad del Bío-Bío, Avenida Collao 1202, Casilla 15-C, Concepción, Chile
[56] Department of Physics & Astronomy, University of Kansas, 1082 Malott, 1251 Wescoe Hall Drive, Lawrence, KS 66045, USA
[57] American Association of Variable Star Observers, 49 Bay State Road, Cambridge, MA 02138, USA
[58] George Mason University, 4400 University Drive, Fairfax, VA 22030 USA
[59] Earth & Planets Laboratory, Carnegie Institution for Science, 5241 Broad Branch Road, NW, Washington, DC 20015, USA
[60] Department of Physics and Astronomy, Vanderbilt University, 6301 Stevenson Center Lane, Nashville, TN 37235, USA
Received 2021 July 30; revised 2022 January 3; accepted 2022 January 6; published 2022 March 14

Abstract

LTT 1445 is a hierarchical triple M-dwarf star system located at a distance of 6.86 pc. The primary star LTT 1445A (0.257 $M_{\odot}$) is known to host the transiting planet LTT 1445Ab with an orbital period of 5.36 days, making it the second-closest known transiting exoplanet system, and the closest one for which the host is an M dwarf. Using Transiting Exoplanet Survey Satellite data, we present the discovery of a second planet in the LTT 1445 system, with an orbital period of 3.12 days. We combine radial-velocity measurements obtained from the five spectrographs, Echelle Spectrograph for Rocky Exoplanets and Stable Spectroscopic Observations, High Accuracy Radial Velocity Planet Searcher, High-Resolution Echelle Spectrometer, MAROON-X, and Planet Finder Spectrograph to establish that the new world also orbits LTT 1445A. We determine the mass and radius of LTT 1445Ab to be 2.87 ± 0.25 $M_{\oplus}$ and $1.304^{+0.067}_{-0.060}$ $R_{\oplus}$, consistent with an Earth-like composition. For the newly discovered LTT 1445Ac, we measure a mass of $1.54^{+0.20}_{-0.19}$ $M_{\oplus}$ and a minimum radius of 1.15 $R_{\oplus}$, but we cannot determine the radius directly as the signal-to-noise ratio of our light curve permits both grazing and nongrazing configurations. Using MEarth photometry and ground-based spectroscopy, we establish that star C (0.161 $M_{\odot}$) is likely the source of the 1.4 day rotation period, and star B (0.215 $M_{\odot}$) has a likely rotation period of 6.7 days. We estimate a probable rotation period of 85 days for LTT 1445A. Thus, this triple M-dwarf system appears to be in a special evolutionary stage where the most massive M dwarf has spun down, the intermediate mass M dwarf is in the process of spinning down, while the least massive stellar component has not yet begun to spin down.

Unified Astronomy Thesaurus concepts: Exoplanets (498); Solar neighborhood (1509); Multiple stars (1081); M dwarf stars (982)

Supporting material: data behind figure, machine-readable table

1. Introduction

Terrestrial exoplanets are difficult to study. Whether one is seeking to measure their bulk densities, search for attendant satellites, or probe their atmospheres, the task is made easier by two factors. First, the host stars must be nearby, so that we might mitigate the cruel dictates of the inverse square law. Second, the stellar mass and radius should be small, so that the ratio of the planetary and stellar quantities is maximized. It is for these reasons that nearby M-dwarf systems are the darlings of the exoplanet menagerie. Fortunately, M dwarfs are abundant, making up approximately 72% of all stars in the stellar neighborhood (Henry et al. 2018). Their dominance among nearby planetary hosts is likewise in evidence. Indeed, of the 16 stars within 15 parsecs that are known to host transiting exoplanets, all but 4 are M dwarfs.

At a distance of 6.53 pc, the closest star known to host transiting exoplanets is HD 219134 (Motalebi et al. 2015; Gillon et al. 2017). Although the two transiting worlds have had their densities measured, they are otherwise largely inaccessible because the parent star is a K dwarf with a radius of 0.778 $R_{\odot}$. However, the star in second place is much more diminutive in stature: LTT 1445A, with a radius of 0.268 $R_{\odot}$ and a mass of 0.257 $M_{\odot}$. At a distance of 6.86 pc (Gaia Collaboration et al. 2016; Lindegren et al. 2021), it is the closest M dwarf known to host a transiting planet. Using data from the Transiting Exoplanet Survey Satellite (TESS; Ricker et al. 2015) and a host of ground-based telescopes, Winters et al. (2019, hereafter W19), published the discovery of LTT 1445Ab, a planet with an orbital period of 5.36 days. Although that planet was presumed to be terrestrial owing to its radius, no measurement of its mass has yet been presented. A mass measurement is crucial for at least two reasons. First, it would constrain the bulk composition of the planet. If the planet proves to be terrestrial, the mass measurement would allow for the determination of the ratio of its iron-and-nickel core to its magnesium-silicate mantle, which in turn could be compared to elemental abundances of the stellar photosphere. Second, future atmospheric studies require a direct estimate of the surface gravity to enable an unambiguous interpretation of data gathered in transmission, as the atmospheric scale height is a combination of the surface gravity, temperature, and mean

[61] Banting Fellow.
[62] NSF Graduate Research Fellow.
[63] NSF Astronomy and Astrophysics Postdoctoral Fellow.
[64] Henry Norris Russell Fellow.
[65] UC Chancellor's Fellow.

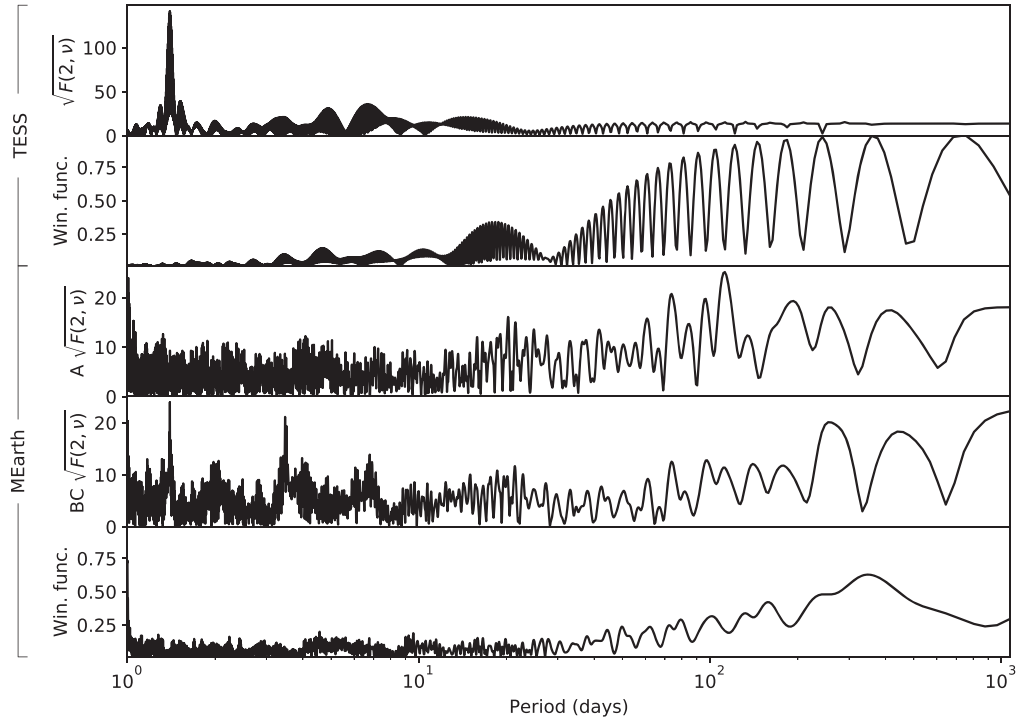

Figure 1. Periodograms and window functions of TESS and MEarth data of LTT 1445. The TESS data (top two panels), which include all three stellar components, exhibit a 1.4 day period. This signal is also seen in the periodogram of the MEarth data for LTT 1445BC (fourth panel), confirming that either the B or C component is the origin of the 1.4 day signal in the TESS data. The peak at 3.5 days represents an alias of the 1.4 day period. The cluster of peaks between 50 and 100 days likely indicates the rotation period of A (middle two panels), but more data are needed for a robust detection of the expected period of 85 ± 22 days. A marginal 6.7 day signal is also seen in both the TESS data and the MEarth data of LTT 1445BC, which we discuss further in Section 4.5.

molecular weight. Intriguingly, LTT 1445A is the most massive member of a resolved triple M-dwarf system. The three stars fall on a line (see Figure 1 from W19), and the stellar orbital plane of stars B and C is viewed edge-on, and hence the entire system may be coplanar.

In pursuit of the mass of LTT 1445Ab, we set out to gather multiepoch radial-velocity (RV) measurements with five high-resolution spectrographs. While that activity was underway, we found a second periodic transit-like signal in the TESS data. Combining the RV and TESS data with ground-based photometric monitoring, we established that indeed a second planet transits LTT 1445A and orbits interior to the known world. In what follows, we describe these findings, along with our measurements of the masses of both worlds.

We briefly summarize the host star system in Section 2, before turning to a description of our photometric and spectroscopic data in Section 3. We present our analysis of these data in Section 4 and their implications in Section 5.

2. Description of the Host Stellar System

The host system, LTT 1445ABC[66] (Luyten 1957, 1980), is a nearby, hierarchical trio of mid-to-late M dwarfs. The preliminary astrometric orbit for LTT 1445BC, presented in W19, indicates an orbital period of 36.2 ± 5.3 yr and a semimajor axis $1\farcs159 \pm 0\farcs076$, which corresponds to an average physical separation of 8.1 ± 0.5 au. As noted in W19, the separation between A and BC appears to have recently begun decreasing, with the most recent value of $7\farcs10$ obtained in 2017, according to data available in the Washington Double Star (WDS) Catalog[67] (Mason et al. 2009). Considering the total mass of the three stellar components and an average angular separation of $5''$ (corresponding to 34 au, calculated using the weighted mean of the parallaxes of A and BC: 145.6917 ± 0.0244 mas), we estimate the period of the A–BC orbit to be roughly 250 years. We refer the reader to Figure 1 in W19, which presents a resolved image of the three stars in the system. We also refer the reader to Table 1 in W19, which lists the astrometry, photometry, and stellar parameters of LTT 1445.

3. Observations

3.1. Photometric Time Series Data

We describe here the photometric time series observations of LTT 1445 by TESS, the MEarth-South telescope array, and the Las Cumbres Observatory telescope network.

3.1.1. TESS Observations

TESS observed LTT 1445 in the first year of its prime mission, which resulted in the discovery of LTT 1445Ab, as described in W19. We included this system in our TESS Guest Investigator program (PI Winters; G03250) target list to gather short-cadence (two-minute) data of the volume-complete sample of M dwarfs with masses $0.1 \leqslant M/M_{\odot} \leqslant 0.3$ within 15 pc (Winters et al. 2021). LTT 1445A and BC were also included in the TESS Input Catalog (TIC) and Candidate Target List (CTL; Stassun et al. 2018) via the Cool Dwarf

[66] Other names for A: TIC 98796344, TOI 455, L 730-18, BD-17 588A, RST 2292A, WDS J03019-1633A, 2MASS J03015142-1635356, Gaia DR2 5153091836072107136, GJ 3193; other names for BC: TIC 98796342, BD-17 588B, RST 2292BC, WDS J03019-1633B, 2MASS J03015107-1635306, Gaia DR2 5153091836072107008.

[67] https://www.usno.navy.mil/USNO/astrometry/optical-IR-prod/wds/WDS

Sample (Muirhead et al. 2018). The LTT 1445 system was reobserved at two-minute cadence in sector 31 from UT 2020 October 22 to November 16, in spacecraft orbits 69 and 70. The system fell on CCD 4 of Camera 2.

As described in the data release notes[68] for sector 31, data collection was paused for 1.4 days between the two orbits to download data, a single momentum dump was conducted halfway through each orbit, and a star tracker anomaly caused the data collection in orbit 70 to end 2.08 days early.

The two-minute cadence data were reduced with the NASA Ames Science Processing Operations Center (SPOC) pipeline (Jenkins et al. 2015, 2016) that was repurposed from the Kepler reduction pipeline (Jenkins et al. 2010). A planet candidate with an approximate radius of $1.5 \pm 0.4\ R_{\oplus}$ was again detected in four transits during sector 31 to have a period of 5.36 days and a transit depth of 2750 ± 191 ppm with a signal-to-noise ratio of 15.2.

A second planet with a 3.12 day period and a transit duration of roughly 45 min was identified in the sector 4 light curve of LTT 1445 by several of us (MHK, IAT, HMS, MO, AS). After the release of the sector 31 light-curve data, we recovered a very shallow transit signal with a period of $P = 3.12$ days. This second planet has not been identified by the TESS planet-vetting team, and thus is not assigned a TOI designation; however, the TESS SPOC algorithm recovered signals at periods of 1.5623 days and 1.5616 days, half that of the expected period, with a multiple event statistic (MES; Jenkins et al. 2002, equivalent to the signal to noise of the transit in the folded light curve) of 6.77 and 5.36 for the sector 4 and 31 data, respectively. To advance to the vetting process, planet candidates must have a SPOC MES larger than 7.1. The SPOC team manually reran their data validation algorithm (Twicken et al. 2018; Li et al. 2019), allowing for both the 1.56 and 3.12 day periods. While the 1.56 day signal was strong, the candidate failed the odd/even transit test at this period. The 3.12 day signal passed the odd/even transit test. The 3.12 day signal consisted of six observed transits in the sector 4 light curve yielding a transit depth of 1554 ± 187 ppm, and eight transits in the sector 31 light curve, yielding a transit depth of 1607 ± 192 ppm. However, the S/N of the light curve was insufficient to use the TESS pixel-level diagnostics to identify which star in LTT 1445 was the origin of the 3.12 day transit signal.

There is no background star from which the transit could originate. W19 compared the position of the system in archival images taken in 1953 to its position at the time the TESS data were taken in 2018. The system's high proper motion (roughly half an arcsecond per year) and the 65 year difference in the images permitted W19 to eliminate the hypothesis that the transit signal originates from a background star coincident with the position of LTT1445 at the TESS epochs. The system has moved only roughly 1″ between the 2018 and 2020 data, so this conclusion remains valid. We are thus confident that the transit signal originates in the LTT 1445 system.

3.1.2. MEarth-South Photometric Monitoring

For the purpose of determining the rotation periods of A and BC, we gathered photometric monitoring observations using MEarth-South (Nutzman & Charbonneau 2008; Irwin et al. 2015) telescope 6 at Cerro Tololo Inter-American Observatory (CTIO), Chile, beginning UT 2019 February 14; observations are ongoing at the time of writing. The data set used in the present analysis includes 330 nights of data ending 2021 October 7. We gathered no observations between 2020 March 10 and 2020 November 4, when CTIO was closed due to the COVID-19 pandemic.

We gathered data in visits of 5×4 s at a cadence of approximately 20 minutes between visits while the target was above 2 airmasses and there were no higher priority observations such as transit follow-up. We obtained a total of 17,987 exposures.

The delivered image quality of the MEarth telescopes can be highly variable over long time baselines, predominantly due to wind shake. Wind at the location of MEarth-South on Cerro Tololo shows a seasonal variation, with stronger and more gusty winds during the winter and spring seasons in particular. FWHM values ranging from approximately 1.7–5.3 pixels were recorded during the time series, where the pixel scale is 0.84 arcsec/pixel. Consequently, while the BC pair is always blended, there is variable blending between A and BC, requiring specialized photometric extraction procedures.

As described in W19, separate apertures of 4.2 pixels in radius were placed on the A and BC components, using a global (full-field) astrometric solution for aperture positioning to avoid drift in the relative positions of the A and BC apertures as a function of the image quality. For the present purpose, we require separate light curves of A and BC, so external comparison stars elsewhere in the field were used rather than the procedure used for the transit follow-up observations in our previous work. The LTT 1445 system is in a sparse field so there were relatively few of these available, and they are fainter than the target stars. Thus, the resulting photometric solutions exhibit higher noise levels and systematic errors than are typical for MEarth data.

The comparison star solutions are unable to correct the effect of variable blending between A and BC, which causes fairly severe systematic errors in the resulting light curves. In order to partly correct this effect, we modified our standard techniques used for periodogram analysis of MEarth data detailed in Newton et al. (2016) to use simultaneous linear decorrelation against both the standard "common mode" term (to correct variable atmospheric precipitable water vapor) and against the FWHM.

The resulting periodograms are shown in Figure 1, where we compare results for the TESS light curve containing all three components with the separate MEarth light curves for A and BC. We also show the periodogram of the observational window function in each case.

The periodogram is plotted in terms of the F-test statistic for the nested model comparison between the null hypothesis of only the baseline detrending with no rotation signal, and the alternate hypothesis where there is also a sinusoidal signal of the given period (further details of this procedure are given in Newton et al. 2016). At a fixed period, this statistic would follow an F distribution $F(2, \nu)$ where the number of degrees of freedom ν is large. Standard results for this distribution show the 1.4 day signal in the MEarth light curve of LTT 1445 BC is highly significant with an F value several hundred above the baseline level in the periodogram.

[68] https://archive.stsci.edu/missions/tess/doc/tess_drn/tess_sector_31_drn47_v02.pdf

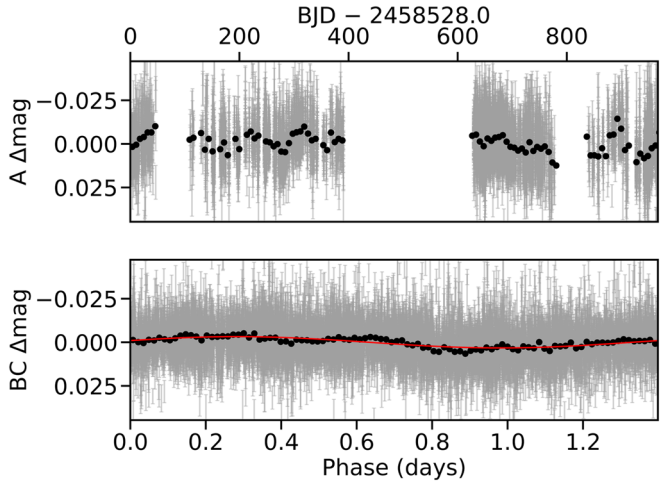

Figure 2. MEarth light curves of LTT 1445A (top) and BC (bottom), phase-folded to the 1.4 day stellar rotation period. The data have been corrected for precipitable water vapor, and outliers have been rejected. The gray points and error bars indicate the individual measurements, while the black points indicate the binned data. The red curve in the bottom panel illustrates the 1.4 day rotation period model for LTT 1445BC. The top panel illustrates that we do not yet have enough data for a robust rotation period detection of LTT 1445A.

(The data used to create this figure are available.)

The 1.4 day signal detected in TESS data and reported previously by W19 is found to originate from BC, as expected based on stellar activity and rotational broadening results presented in the previous paper, but this has now been resolved observationally. The 1 day^{-1} alias of this signal is also seen close to 3.5 days. No clear rotational modulation signal meeting our quality criteria (see Newton et al. 2016) is yet detected in LTT 1445A, but the periodogram shows power at long periods between approximately 40 and 150 days and the corresponding alias period close to 1 day. Based on the observed activity level and mass of this star, a rotation period around 85 ± 22 days would be expected (calculated using the empirical relation in Newton et al. 2017) but has yet to be detected in the observations. We show the MEarth light curves for LTT 1445A and BC in Figure 2.

3.1.3. MEarth-South Transit Follow-up Observations

We also performed follow-up observations with MEarth-South spanning times of the transit of planet b. Because MEarth is able to spatially resolve star A from stars BC, these data serve to confirm that planet b indeed transits star A. As discussed above in Section 3.1.2, MEarth observations of the LTT 1445 system are extremely sensitive to image quality due to the components being barely resolved in the data. Additionally, due to the short exposure time, atmospheric scintillation noise is severe and increases with airmass. Consequently, although we observed several transits of LTT 1445Ab for follow up, the majority of these were of poor quality, and all but one were rejected for the final analysis.

Our analysis includes a single full transit observed on UT 2019 September 2 using seven telescopes. Otherwise, the observational strategy and reduction techniques were identical to those described in W19 and are not repeated here. A total of 3935 data points were gathered during this time series, and the resulting light curve is shown in the top panel of Figure 3.

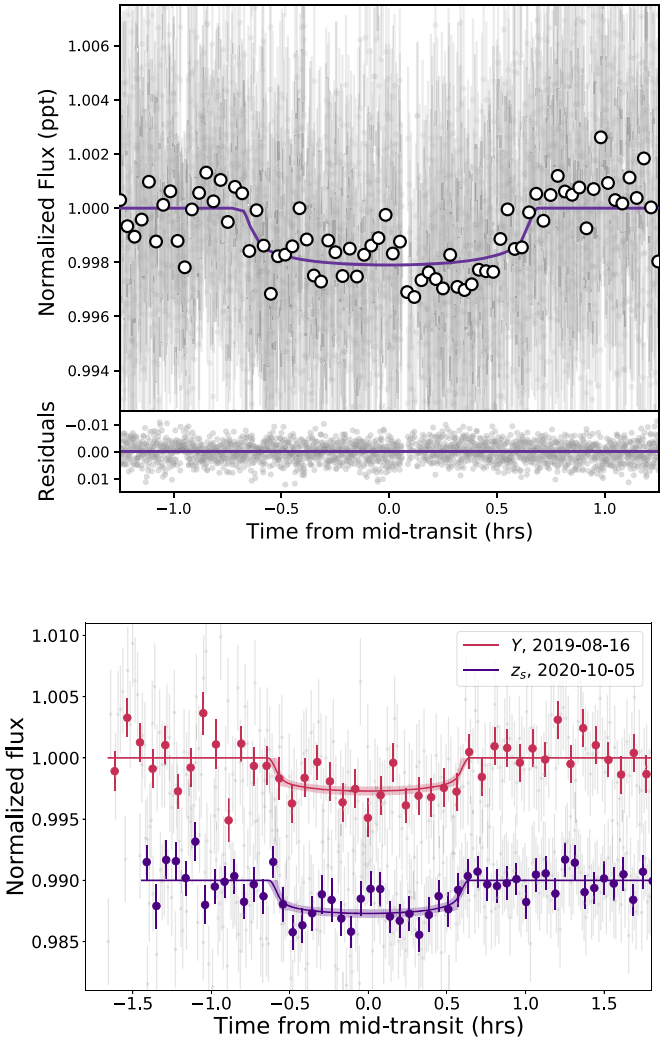

Figure 3. Transits of LTT 1445Ab measured from ground-based data. The top panel shows the transit of LTT 1445Ab as observed by MEarth-South on UT 2019 September 2 using seven telescopes. The bottom panel shows two transits of LTT 1445Ab as observed by LCOGT.

Because the expected transit depth of the 3.12 day planet candidate was below the detection limits of the MEarth array, we did not attempt observations to confirm it with MEarth.

3.2. LCOGT Transit Follow-up Observations

We observed three full transits of LTT 1445Ab from the Las Cumbres Observatory Global Telescope (LCOGT; Brown et al. 2013) 1.0 m network. We observed a full transit on UT 2019 August 16 in the Panoramic Survey Telescope and Rapid Response System (Pan-STARRS) Y-band from the CTIO node using 30 s exposures, and a full transit on UT 2020 October 8 in the Pan-STARRS z-short band from the McDonald Observatory node using 10 s exposures. A full transit was observed on UT 2019 July 16 from the South Africa Astronomical Observatory node in the Pan-STARRS Y-band using 30 s exposures. However, we ultimately chose not to include this observation in the analysis because only a few minutes of nominal posttransit baseline were observed, resulting in an unclear time of egress and thus a depth measurement that is not well constrained. We used the `TESS Transit Finder`, a customized version of the `Tapir`

Table 1
Radial Velocities for LTT 1445A

BJD[a] (days)	v_{rad}[b] (m s^{-1})	σ (m s^{-1})	Spectrograph
2458546.500296	−5457.74	1.31	HARPS
2458547.501338	−5463.53	1.16	HARPS
2458548.500633	−5460.85	1.36	HARPS
2458555.506869	−5455.18	1.29	HARPS
2458556.505906	−5453.54	1.16	HARPS

Notes.
[a] Barycentric Julian Date of midexposure, in the TDB time-system.
[b] Barycentric radial velocity.
(This table is available in its entirety in machine-readable form.)

software package (Jensen 2013), to schedule our transit observations. The 4096 × 4096 LCOGT SINISTRO cameras have an image scale of 0.″389 per pixel, resulting in a 26′ × 26′ field of view. The images were calibrated by the standard LCOGT `BANZAI` pipeline (McCully et al. 2018), and photometric data were extracted with `AstroImageJ` (Collins et al. 2017). The UT 2019 August 16 images were (unintentionally) mildly defocused and had typical stellar point-spread-functions with a FWHM of roughly 3.″8. Circular apertures with radius of roughly 2.″7 were used to extract the differential photometry. We estimate that about 2% of the flux in the target star aperture is from the nearby pair LTT 1445BC. The UT 2020 October 8 images were very slightly defocused and had typical stellar point-spread-functions with a FWHM of roughly 2.″1. Circular apertures with radius about 3.″5 were used to extract the differential photometry. We estimate that about 1.3% of the flux in the target star aperture is from the nearby pair LTT 1445BC. For all observations, we used a single comparison aperture around the nearby pair LTT 1445BC to extract the light curve of LTT 1445Ab. The light curves are presented in the bottom panel of Figure 3.

Using the LCOGT 1.0 m network and an ephemeris extracted from TESS sector 4 data, we attempted to recover the 3.12 day transit signal on six epochs in 2019 and 2020. However, the updated ephemeris based upon the combination of the sector 4 and 31 data shows that those observations were typically 5 hr late and do not span the times of transit.

3.3. Spectroscopic Data

We combined 136 RVs of LTT 1445A from five high-resolution spectrographs taken over roughly two years. Here we describe the instruments in alphabetical order, as well as the methods used to measure the RVs and their uncertainties. We list the RVs and their uncertainties in Table 1.

3.3.1. ESPRESSO

We acquired 19 spectra of LTT 1445A with the Echelle Spectrograph for Rocky Exoplanets and Stable Spectroscopic Observations (ESPRESSO) spectrograph (Pepe et al. 2021) on the Very Large Telescope (VLT) from UT 2020 July 04 to September 03. ESPRESSO is an ultrastable, fiber-fed echelle spectrograph with resolving power $R = 140{,}000$ in the high-resolution (1-UT) configuration and a wavelength range of 378.2–788.7 nm. We used integration times of 900 s and we employed the slow (100 kpx s^{-1}), 2 × 1 binning readout mode. We elected not to use the simultaneous wavelength calibration; thus, the calibration fiber was set on sky. The S/N of the spectra ranges between 58 and 142 at 650 nm, with an average of 104.

We derived the RVs using the χ^2-minimization template-matching method described in Astudillo-Defru et al. (2015). The stellar template was built from the median of the individual spectra, accounting for the ESPRESSO design that creates two individual images (slices) of the same spectral order. To compute the RVs, we discarded echelle orders below order 15 (30 slices) due to the low flux, as well as zones containing telluric features. RV uncertainties were computed following the methods described in Bouchy et al. (2001) and range between 0.15 m s^{-1} and 0.32 m s^{-1}, with an average uncertainty of 0.20 m s^{-1}.

3.3.2. HARPS

We acquired 45 spectra of LTT 1445A with the High Accuracy Radial Velocity Planet Searcher (HARPS) spectrograph (Mayor et al. 2003) on the La Silla 3.6-m telescope from UT 2019 March 04 to October 21. HARPS is a fiber-fed echelle spectrograph with resolving power $R = 115{,}000$ and a wavelength range of 378-691 nm. We employed integrations times of 900 s, and the spectra were read out in slow mode (104 kpx s^{-1}), except for one spectrum acquired on 2019 September 12, which had an exposure time of 1500 s. We found that for seven of our spectra we had inadvertently observed the BC component, as evidenced by the Hα emission. We discarded these from the RV analysis, but these spectra later proved to be a blessing in disguise, as they allowed us to investigate the rotational broadening of the B and C components (see Section 4.5). The calibration fiber was set on sky. The science fiber provides S/Ns between 26 and 60 at 650 nm, with an average of 48. As with ESPRESSO, we derived the RVs by template matching, and we estimated the uncertainties following the methods of Bouchy et al. (2001); these range between 1.06 m s^{-1} and 2.86 m s^{-1}, with an average uncertainty of 1.44 m s^{-1}. We allowed for a separate RV zero-point offset for the 2019 February data because of the roughly four-month time span between those data and the later observations.

We also measure the Ca II H and K emission (S activity index) and proceed to calculate a value of $\log(R'_{HK}) = -5.413 \pm 0.118$. Following Astudillo-Defru et al. (2017), we estimate a rotation period of 79 ± 15 days, in agreement with the estimated rotation period of 85 ± 22 days noted above.

3.3.3. HIRES

We acquired 39 spectra of LTT 1445A with the High-Resolution Echelle Spectrometer (HIRES) on the 10 m Keck telescope on Maunakea, Hawaii, on nights between UT 2019 August 14 and 2020 February 28. HIRES is an optical echelle spectrograph with resolving power $R \approx 55{,}000$ (Vogt et al. 1994). We used the standard procedures of the California Planet Search (CPS; Howard et al. 2010) to make the observations and reduce the spectra. This includes the use of an iodine cell to calibrate the wavelength solution and point-spread function of HIRES, as well as a long slit (the "C2" decker) to measure and subtract contemporaneous sky spectra. We used an image rotator to orient the field so that light from LTT 1445A went through the slit, and light from LTT 1445BC did not. The HIRES spectra span the wavelengths 364–790 nm with our CPS setup, but the RVs were computed from the

wavelength range 500–630 nm because that region is calibrated by the iodine. We used integration times of 900 s, which resulted in S/Ns of 100–170 per pixel on blaze near 550 nm. We computed relative RVs using the method descended from Butler et al. (1996). The HIRES RVs have internal uncertainties between 1.3 m s^{-1} and 2.0 m s^{-1}, with an average uncertainty of 1.5 m s^{-1}.

3.3.4. MAROON-X

We used the MAROON-X spectrograph (Seifahrt et al. 2016, 2018, 2020) on the 8.1-m Gemini-North telescope to measure RVs of LTT 1445A during three observing runs of two weeks each between 2019 December and 2020 November. MAROON-X is a stabilized, fiber-fed echelle spectrograph with resolving power $R \simeq 85{,}000$ and a wavelength range of 500–920 nm in two camera arms. MAROON-X has demonstrated an RV stability of at least 30 cm s^{-1} over the span of a few weeks during its first year of operations (Seifahrt et al. 2020) and has recently been used to determine a precise mass of the nearby transiting rocky planet Gl 486b (Trifonov et al. 2021).

We acquired 27 spectra of LTT 1445A over eight nights during the science verification and commissioning phase of the instrument in 2019 December. The simultaneous calibration was not operational during these first observations, so bracketing wavelength calibration exposures were taken to track the instrumental drift. The lack of simultaneous calibration likely limits the instrumental precision of these data to approximately 1 m s^{-1}. Moreover, we found that 7 of the 27 spectra in two consecutive nights in 2019 had low S/N and also showed abnormal chromatic index and differential line widths in MAROON-X's blue arm. Some of these spectra lead to RV outliers and thus all seven spectra were subsequently dropped from the RV analysis. Due to their low S/N and thus larger individual RV uncertainty, their contribution to the nightly mean was small and did not significantly change the final RV data point for the night.

We gathered an additional 20 spectra over 17 nights in 2020 September and November. We find only a single night with notable stellar activity in this data set. Because the RV measurement from this one night does not present as a clear outlier, we included this data point in the RV analysis.

We used integration times of 600 s in 2019 and 300 s in 2020. In 2019, the peak S/N per 1D pixel ranges between 60 and 190 at 640 nm in the blue arm and between 140 and 430 at 800 nm in the red arm, with a widespread distribution depending on seeing conditions. In 2020, we find peak S/Ns ranging between 50 and 95 at 640 nm in the blue arm and between 130 and 250 at 800 nm in the red arm.

We reduced the MAROON-X raw data using a custom `Python 3` pipeline based on tools previously developed for the Cryogenic Infrared Echelle Spectrograph (Bean et al. 2010). The wavelength and instrumental drift solution of MAROON-X is based on a stabilized Fabry–Perot etalon (Stürmer et al. 2017) in conjunction with a ThAr lamp for the initial measurement of the gap size and chromatic dispersion of the etalon. In early 2020, the simultaneous calibration fiber of MAROON-X became operational, allowing for a robust order-by-order drift correction at the sub–m s^{-1} level. Barycentric corrections were computed using the `barycorrpy` code (Kanodia & Wright 2018) from weighted averages based on MAROON-X's white-light exposure meter.

We computed the RVs using `serval` (Zechmeister et al. 2018), which employs a χ^2-minimization algorithm based on matching an empirical template to each order at each epoch. The template is constructed from the data set itself as a weighted average of all observations. A telluric mask is used to exclude telluric absorption features deeper than about 1%, both in the construction of the template and in each epoch. Typical uncertainties derived by `serval` are based on the interorder dispersion of the RVs and range from 0.25 m s^{-1} for the highest S/N of 430 in the red channel to 1.6 m s^{-1} for the lowest S/N of 60 in the blue channel. To increase the S/N for robust RV calculations, we combined blue and red arm observations as well as multiple back-to-back observations per night into nightly epoch means and propagated uncertainties based on the spread of the individual measurements. These final uncertainties range from 0.4 to 1.4 m s^{-1} in 2019 and 0.4 to 1.0 m s^{-1} in 2020, with an average uncertainty of 0.8 and 0.6 m s^{-1}, respectively.

Because of an instrument intervention that took place after the 2019 commissioning run, which introduced changes to both the etalon as well as the spectral format of the blue arm, we treat the data from 2019 and 2020 as independent data sets with distinct RV offset parameters.

3.3.5. PFS

We acquired 25 spectra (15 when binned by night) of LTT 1445A with the Planet Finder Spectrograph (PFS; Crane et al. 2006, 2008, 2010), mounted on the 6.5 m Magellan II telescope at Las Campanas Observatory in Chile, from UT 2019 July 20 to 2020 November 4. PFS covers 391–734 nm, and the subsequent RVs are calibrated using the iodine method. The default 0.″3 slit provides a resolving power $R \simeq 127{,}000$. Integration times ranged from 960 to 1500 s resulting in S/Ns between 40 and 70 at the peak of the blaze around 600 nm. All PFS spectra are reduced and analyzed using a custom `IDL` pipeline based on Butler et al. (1996) that regularly delivers sub–m s^{-1} precision. We binned observations taken sequentially to improve the S/N for robust RV calculations. The RV uncertainties in our nightly binned RVs ranged between 0.48 m s^{-1} and 0.83 m s^{-1}, with an average uncertainty of 0.63 m s^{-1}.

4. Analysis

Because of the complex nature of the TESS light curve, we used a combination of `exoplanet` (Foreman-Mackey et al. 2017) and `ExoFASTv2` (Eastman et al. 2019) for our light-curve modeling: We first used `exoplanet` to fit and remove the photometric modulation in the TESS light curve using a Gaussian Processes (GP) regression model via `celerite` while preserving the transit signals of the two planets. We then used `ExoFASTv2`, which does not use GPs, to simultaneously fit the RV data and the detrended transit data from `exoplanet`. We also performed an independent RV-only analysis that included a GP regression to account for stellar activity that could affect the uncertainties of the planetary masses.

We will know the masses and radii of these planets only as well as we know these values for their host star. We estimate a mass of $0.257 \pm 0.014\ M_{\odot}$ for the host star using the mass–luminosity relation in the K band by Benedict et al. (2016) and then use a single-star mass–radius relation (Boyajian et al. 2012)

to estimate a stellar radius of $0.268 \pm 0.027\ R_{\odot}$. We calculate the bolometric corrections in K (Mann et al. 2015) and in V (Pecaut & Mamajek 2013), along with their respective bolometric luminosities. We adopt the mean of the two bolometric luminosities and then use the Stefan–Boltzmann law to calculate an effective temperature $T_{\rm eff}$ of 3337 ± 150 K for LTT 1445A. We adopt a metallicity [Fe/H] of -0.340 ± 0.090 dex from Neves et al. (2014), which is measured using HARPS data. We updated the parallax of LTT 1445A to that of the Gaia Early Data Release (EDR3; Gaia Collaboration et al. 2016; Lindegren et al. 2021) for our estimates of the star's mass, radius, and effective temperature, but these values did not change significantly from those reported in W19. We use these stellar parameters of LTT 1445A as priors for the light curve and RV modeling described below.

4.1. Light-curve Modeling with `exoplanet`

The presence of other objects in the TESS aperture can dilute the transit depth of the planet, which is measured from the light curve. If the additional objects have identifiers and TESS magnitudes in the TESS Input Catalog (TICv8.1; Stassun et al. 2019), the SPOC pipeline calculates a dilution (i.e., contamination) factor and performs a correction to the final light curve (Stumpe et al. 2012). For the sector 4 data, the SPOC contamination value of 0.4849 is very close to our estimated value of 0.480 ± 0.013, which is calculated from T mags estimated from an M-dwarf-specific relation (W19). For the sector 31 light curve, the SPOC contamination value is 0.42003, which is significantly different. The difference is partly due to an updated T mag for LTT 1445A of $T = 8.843$ mag in the TICv8.1, compared to $T = 8.64$ mag from an earlier TIC version. However, the TICv8.1 also appears to have a duplicate entry for LTT 1445BC, one from the 2MASS cross match (TIC 98796342) with $T = 8.554$ mag and the other from the Gaia DR2 cross match (TIC 651819442) with $T = 11.558$ mag. Thus, the SPOC dilution value in the sector 31 light curve is an overestimate of the amount of contaminating light from the BC components. As in W19, we removed the SPOC dilution value and imposed our own.

As in W19, we did not include the third transit of LTT 1445Ab in sector 4 in our analysis because the light-curve baseline showed a strong slope at egress; we note that this transit was also omitted from the results in the SPOC DV report. The third transit of LTT 1445Ac in the sector 4 light curve was not observed, as it occurred during the communication failure. The fourth transit occurred during the brief chunk of light curve right before the data download. Our GP did not fit properly over such a small span of data, so in the interest of working with uniformly processed data, we omitted this transit from our analysis. The third transit of the 5.36 day planet in the sector 31 data occurred during the pause in data collection while the data were being downloaded and was thus not observed. The star tracker anomaly reported for sector 31 did not affect the transits of either planet.

We used the python package `exoplanet` (Foreman-Mackey et al. 2019), which employs probabilistic methods to model exoplanet transit and radial-velocity data sets. It has the additional capability to incorporate GP with `celerite` (Foreman-Mackey et al. 2017) and limb-darkened light curves with `starry` (Luger et al. 2018). We used the SPOC-generated Pre-Search Data Conditioning Simple Aperture Photometry (PDCSAP) light curve (Smith et al. 2012; Stumpe et al. 2012, 2014), corrected with our calculated dilution factor. Before fitting, we removed positive outliers (flares) that deviated by more than 3 times the median absolute deviation of the PDCSAP light curve. While we do not know from which star the flares originate, recent work on nearby mid-to-late M dwarfs (see, e.g., Medina et al. 2020) indicates that rapidly rotating stars flare far more frequently. Thus, we suspect that many of the flares originate from either or both of the B or C components.

We model the stellar rotational modulation, as well as any other possible systematics, with a GP. The GP kernel is the sum of two simple harmonic oscillators, which has been shown to be an appropriate kernel for data that are quasiperiodic in nature (Angus et al. 2018), such as the observed rotational modulation in the light curve of LTT 1445ABC. To model the planetary transits, we used a limb-darkened transit model and a Keplerian orbit. We used the same model, priors, GP hyperparameters, and methods for the fit as described in W19. We measure planet-to-star radius ratios of 0.037 ± 0.005 and 0.047 ± 0.006 for LTT 1445Ac and LTT 1445Ab in the TESS sector 4 light-curve data and ratios of 0.035 ± 0.009 and 0.042 ± 0.007 for the respective planets in the TESS sector 31 light-curve data.

We note that the 1.4 day rotation signal has evolved in the two years that elapsed between sector 4 and 31. While the period of the modulation is the same, the semiamplitude of the variability has roughly doubled from 1.475 ± 0.302 ppt in the sector 4 light curve to 3.027 ± 0.401 ppt in the sector 31 light curve. This increase in the semiamplitude is likely due to a change in the morphology of the starspot groups leading to a larger hemisphere-integrated asymmetry in sector 31. We show our GP fit to the TESS light-curve data for both sector 4 and 31 in Figure 4.

4.2. Global Modeling with `ExoFASTv2`

We perform a simultaneous global fit of the TESS light-curve and radial-velocity data using `ExoFASTv2` (Eastman et al. 2019). `ExoFASTv2` is a suite of `IDL` routines that simultaneously fits exoplanetary transit and radial-velocity data using a differential Markov Chain Monte Carlo (MCMC) code. We include the TESS light curves from sectors 4 and 31, and we use 134 RVs from the five spectrographs. We used as input for the `ExoFASTv2` the output light-curve data from `exoplanet` with the stellar variability removed. In order to allow for the propagation of the uncertainty in the dilution that was corrected by the `exoplanet` fit, we allow for a residual dilution, with a prior centered on zero with $\sigma = 0.013$.

Because we derived the stellar parameters as described in Section 2, we did not include a spectral energy distribution in the fit, and we disabled the default Modules for Experiments in Stellar Astrophysics (MESA) Isochrones and Stellar Tracks (MIST) stellar evolutionary models that use isochrones to constrain the stellar parameters. We placed Gaussian priors on the stellar mass, radius, effective temperature, and metallicity that were equal to the uncertainties noted above in Section 4. We interpolated the quadratic limb-darkening coefficients in Table 15 of Claret (2017) to the effective temperature of LTT 1445A, which we imposed with a Gaussian prior with a standard deviation of 0.10. While the atmospheric models used to derive the limb-darkening tables are questionable for low-mass stars such as LTT 1445A, the impact is likely to be negligible due to the low precision of the TESS light curve.

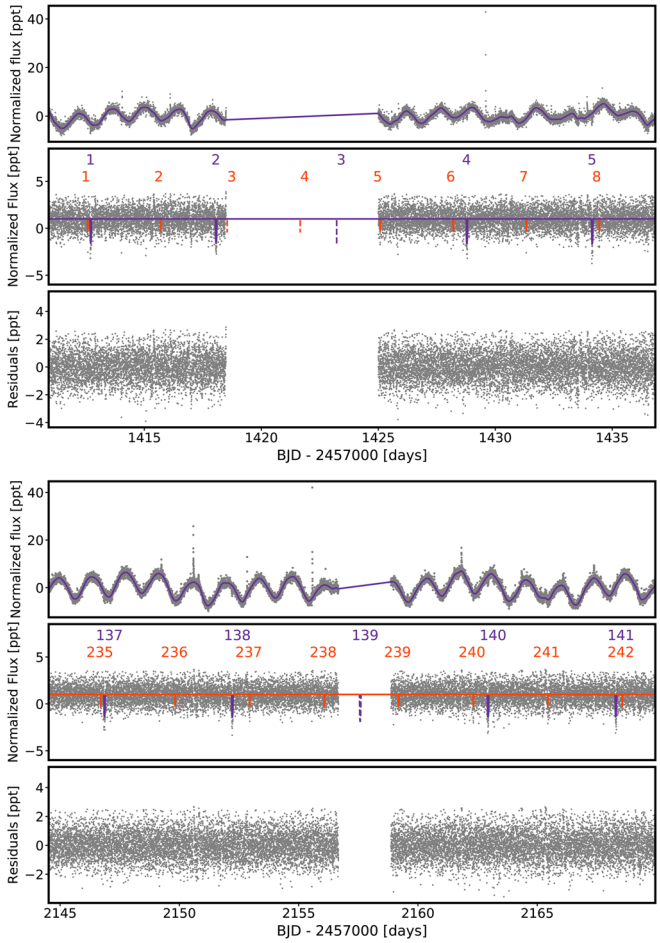

Figure 4. The TESS PDCSAP light curves from sector 4 (top 3 panels) and 31 (bottom 3 panels) data. The top panels of each plot are the nondetrended light curves from each sector of data, which show evidence of flares and rotational modulation due to stellar spots on either the B or C component. The purple lines indicates the fits to the modulations. The middle panels of each plot show the residual data after the removal of the stellar variability with GP regression; the planetary transit models for the 5.36 day planet (purple line) and 3.12 day planet (orange line) are overplotted. The dotted lines indicate transits that occurred during a data download, and which were not observed. The bottom panels of each plot illustrate the light curves with planetary transits and stellar variability removed.

We include a slope term to account for a change in the RVs of LTT 1445A due to the stellar A–BC orbit. We estimated the magnitude of the RV slope as follows. Because the maximum change in RVs over the 643 day time span of our data is dependent upon the eccentricity of the orbit, we explored which eccentricities would result in a stable configuration for the A–BC orbit. The stability criterion for hierarchical triple star systems from Harrington (1972) requires the eccentricity of the outer (A–BC) orbit and the ratio of the semimajor axes of the inner (B–C) and outer orbits. We investigated eccentricities 0 to 0.9 and semimajor axes of 1″ (from the preliminary astrometric orbit for LTT 1445BC reported in Winters et al. 2019) and 5″ (the mean separation noted for LTT 1445A-BC in Section 2), respectively, to estimate that retrograde motion orbits with eccentricities less than 0.45 would be stable. Therefore, we estimate that an orbital period of 253 yr for LTT 1445A-BC would result in a drift in our RV data with values between 0.0002 m s^{-1} day^{-1} for a circular orbit to 0.25 m s^{-1} day^{-1} for an eccentric ($e = 0.45$) orbit. We ran two separate ExoFASTv2 fits, one that included the term for the slope, and one that did not. ExoFASTv2 provides statistical metrics, such as the Bayesian Information Criterion (BIC; Schwarz 1978) and Akaike Information Criterion (AIC; Akaike 1974), for model fits. Both metrics are functions of the number of parameters being fit and the maximum ln(likelihood) from the MCMC sample, while the BIC also considers the number of data points being fit. The better model has the smallest algebraic value of AIC or BIC. The fit that included the slope term for the RVs was slightly preferred over the flat RV fit, with BIC and AIC values of −22,202 and −22,424, respectively, for the model with no slope, compared to values of −22,209 and −22,437 for the model with the slope. We thus included the RV slope term in all of our models.

We rejected flat models (i.e., any instances where an expected transit was not found) in order to prevent the fit from running away, which can happen in the hotter chains when using parallel tempering. We required the number of independent draws to be greater than 1000 and determined that, with a Gelman–Rubin statistic (Gelman & Rubin 1992) of 1.0090 in the worst case, the chains were well mixed.

We initially allowed the radius of the 3.12 day planet to be unconstrained but found that grazing geometries were permitted, indicating that the light curve can set only a lower limit on the planet's radius and an upper limit on its inclination. Similar to Rodriguez et al. (2018), we imposed a constraint on the radius of the 3.12 day planet based on the mass–radius relations by Chen & Kipping (2017). The impact is that this prior sets an upper limit on the planet radius (resulting from the measured planetary mass, informed by the RVs), while the lower limit on the planet radius is set from the observed depth of the transit. We emphasize that our data do not permit us to directly determine the radius of the 3.12 day planet. Although we state the value we determine by employing the Chen & Kipping (2017) prior, the planet radius could be much larger and should be determined by gathering data of greater precision, which would permit the determination of the four points of contact (if they exist). In Table 3, we have flagged all quantities that are affected by this prior.

In principle, if the radius from the Chen & Kipping (2017) relation were inconsistent with the lower limit from the transit, using this relation could bias the mass of the 3.12 day planet. To ensure that was not the case, we used ExoFASTv2 to run a two-planet fit of only the RV data. We found that the resulting RV semiamplitude of LTT 1445Ac is in agreement with both that from our ExoFASTv2 global model fit with the radius constraint imposed, and the separate RV+GP fit we describe in Section 4.4.

Finally, we note that ExoFASTv2 rejects any samples where the planets' projected orbits cross into each other's Hill spheres, with the intention of constraining both planets' eccentricity by rejecting unstable configurations. While this is a reasonable approximation, it is not a substitute for a detailed analysis of the long-term stability of the system, which is beyond the scope of this work.

4.3. Confirmation of the 3.12 Day Planet

Because our only detection of the transits of the 3.12 day planet is from the TESS light-curve data, in which the light from all three stars is blended together, the light curve itself does not prove that the planet orbits star A. Instead the proof

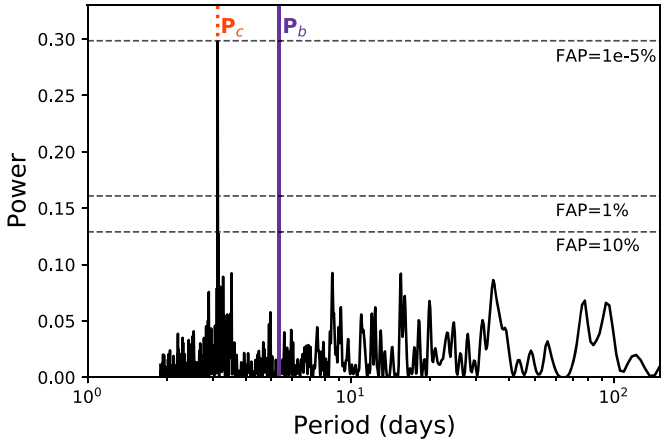

Figure 5. Lomb–Scargle periodogram of the residuals from the 5.36 day planet fit to the RV data of LTT 1445A. False alarm probabilities of 10%, 1% and 1×10^{-5}% are noted (black dashed lines), as are the orbital periods for the 3.12 and 5.36 day period planets (dotted and solid orange and purple lines, respectively). A highly significant peak at 3.12 days is evident, which confirms that the 3.12 day planet also orbits LTT 1445A.

comes from our RVs of LTT 1445A. We first ran a global `ExoFASTv2` fit using both sectors of TESS data and all of the RVs, accounting for only the confirmed 5.36 day planet. We added the RV jitter output from the global model in quadrature with the uncertainties on the RV residuals to properly weight the uncertainties from each instrument. We then created a Lomb–Scargle (L–S) periodogram using the L–S tool (VanderPlas & Ivezić 2015) in `astropy` (Astropy Collaboration et al. 2013, 2018), which we show in Figure 5. There is a peak at 3.12195 days with maximum L–S power at 0.298. The L–S False Alarm Probability (FAP) of a peak at this power is 1.06×10^{-5}%, indicating high significance of the signal and that indeed the 3.12 day planet also transits the primary star of LTT 1445.

We included the second planet in our global model to explore whether the addition of the second planet to our model would improve the fit to the data, under the assumption that it transits the primary star. The results indicate that the two-planet model is preferred over a single-planet model via the BIC and AIC metrics (BIC: −21,981 versus −22,209; AIC: −22,169 versus −22,437 for the one- and two-planet models, respectively). In Section 4.4, we conduct an independent analysis of the RV data using a GP to account for stellar activity, and similarly find that the two-planet model is strongly preferred.

We thus adopt the two-planet model as the most appropriate description of the data and list the median values of the fit parameters from our global `ExoFASTv2` model for both planets in Table 3. We show the resulting transit and RV plots for each planet in Figures 6 and 7.

4.4. Radial-velocity Modeling with a Gaussian Process

Active regions on the surface of a rotating star may produce nonorbital RV signals due to both the magnetic suppression of the net convective blueshift of the photosphere, and through the effect of spots downweighting portions of the stellar velocity field on the visible hemisphere of the star (Meunier et al. 2010). The temporal evolution of these activity signals can be detrimental to the recovery of accurate planetary signals if not properly accounted for. Here we assess the impact of stellar activity in our RV data by explicitly treating stellar activity

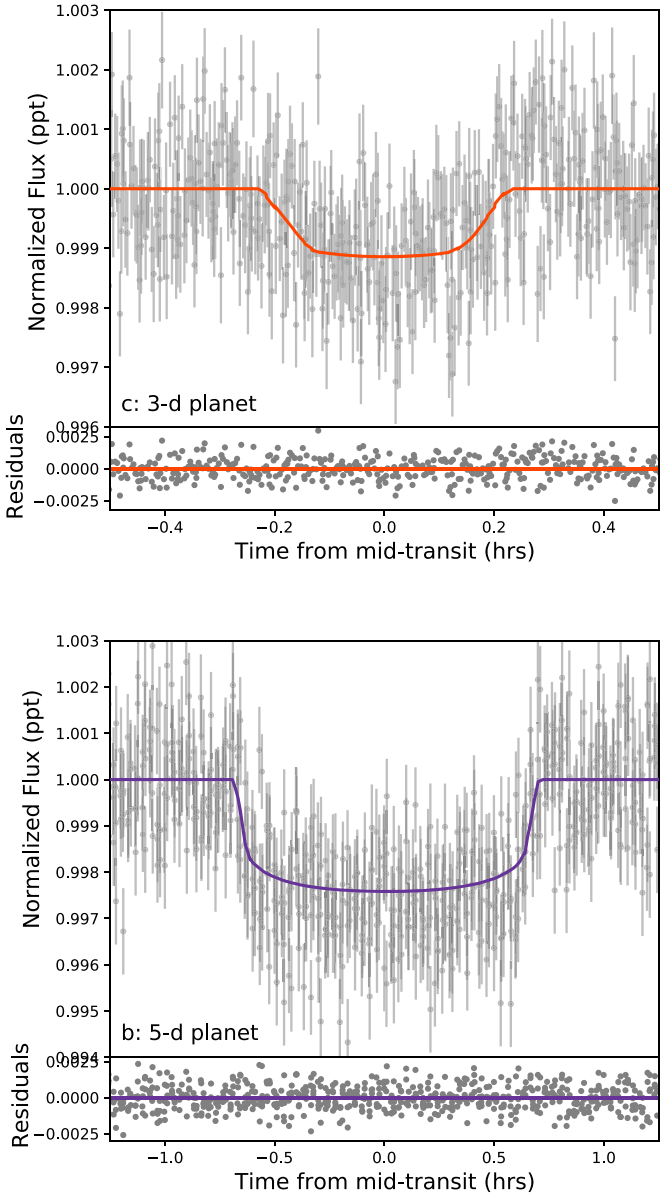

Figure 6. Transits of LTT 1445Ac (top) and LTT 1445Ab (bottom) observed with TESS. The data have been deblended to remove any signal from the stellar BC components and are shown in gray, while the orange and purple lines indicate the models for LTT 1445Ac and LTT 1445Ab.

with a GP regression model component (e.g., Haywood et al. 2014; Rajpaul et al. 2015). Specifically, we model temporal correlations from rotationally modulated magnetic activity using a quasiperiodic GP following the methodology of Cloutier et al. (2017, 2020a, 2020b). To summarize, we adopt a separate quasiperiodic GP for each RV spectrograph due to their unique noise properties and the inherently chromatic nature of stellar activity. For each spectrograph indexed by s, the quasiperiodic covariance kernel is

$$k_{sij} = a_s^2 \exp\left[-\frac{(t_i - t_j)^2}{2\lambda^2} - \Gamma^2 \sin^2\left(\frac{\pi|t_i - t_j|}{P_{\rm GP}}\right)\right], \quad (1)$$

where a_s is the covariance amplitude for spectrograph s, λ is the exponential timescale related to the lifetime of active regions, Γ is the coherence parameter, and $P_{\rm GP}$ is the periodic timescale related to the stellar rotation. We also fit an additive

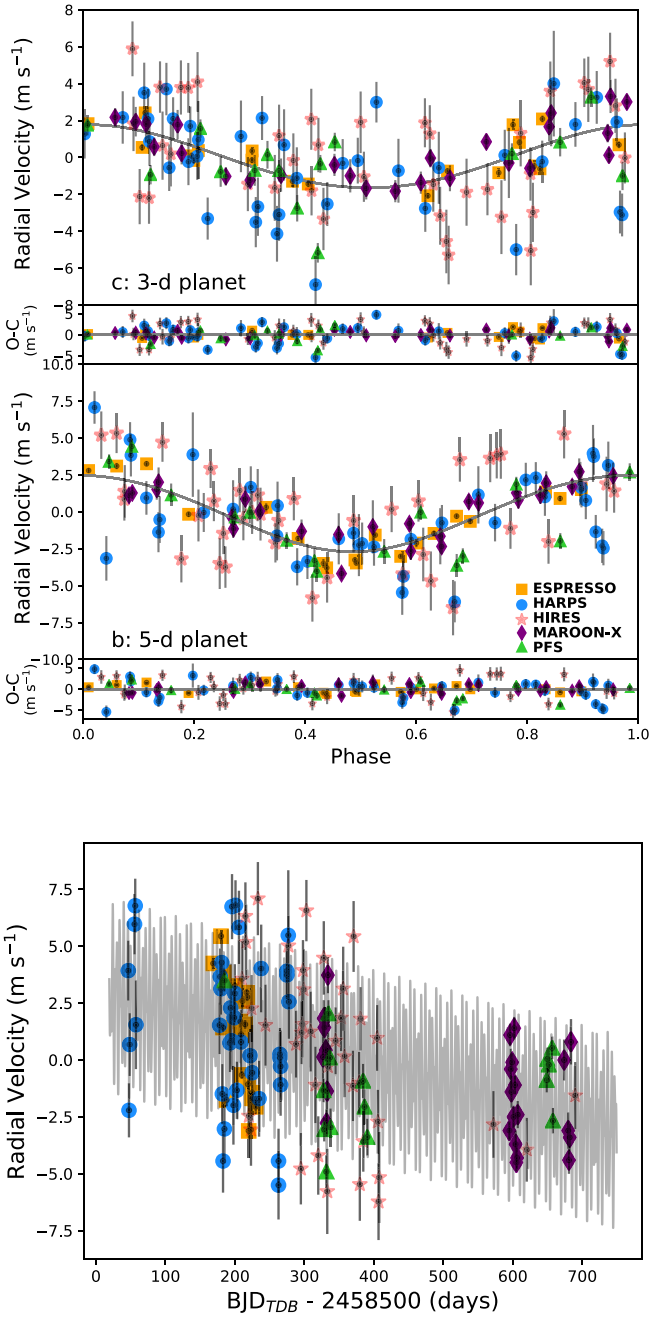

Figure 7. RV orbital plots and residuals from the global ExoFASTv2 two-planet fit. In the top panel, we show the RV data folded at the 3.12 day period (and corrected for the 5.36 day planet, and the slope), with the model for the 3.12 day planet overplotted in gray; residuals to the fit of both planets are shown underneath, phase-folded to the 3.12 day planet period. Similarly, in the third panel, we show the RV data folded at the 5.36 day period (and corrected for the 3.12 day planet, and the slope), with the model for the 5.36 day overplotted in gray; residuals to the fit of both planets are shown underneath, phase-folded to the 5.36 day planet period. The data from ESPRESSO are plotted as orange squares, HARPS as blue circles, HIRES as pale red stars, MAROON-X as purple diamonds, and PFS as green triangles. The bottom panel illustrates the unphased RV data, where the gray curve indicates the combination of the 3.12 day and 5.36 day planet models and the linear slope due to the orbit of LTT 1445A about BC.

scalar jitter $\sigma_{s,\mathrm{RV}}$ for each spectrograph to account for any excess uncorrelated noise. The hyperparameters $\{\lambda, \Gamma, P_{\mathrm{GP}}\}$ are all directly related to the active regions themselves and are therefore independent of the spectrograph. As such, these hyperparameters are shared among each spectrographs GP model.

Table 2
RV + GP Priors

Parameters	Prior
GP Hyperparameters	
$\log a_s/(\mathrm{m\ s^{-1}})$	$\mathcal{U}(-5, 5)$
$\log \lambda/(\mathrm{days})$	$\mathcal{U}(\log 1, \log 1000)$
$\log \Gamma$	$\mathcal{U}(-3, 3)$
P_{GP} [days]	$\mathcal{N}(85, 22)$
LTT 1445Ab RV Parameters	
P_b [days]	$\mathcal{N}(5.358766, 0.000004)$
$T_{0,b}$ [BJD]	$\mathcal{N}(2458412.7085, 0.0004)$
$\log K_b/(\mathrm{m\ s^{-1}})$	$\mathcal{U}(-3, 3)$
$h_b = \sqrt{e}\cos\omega$	$\mathcal{U}(-1, 1)$
$k_b = \sqrt{e}\sin\omega$	$\mathcal{U}(-1, 1)$
LTT 1445Ac RV Parameters	
P_c [days]	$\mathcal{N}(3.123904, 0.000004)$
$T_{0,c}$ [BJD]	$\mathcal{N}(2458412.5816, 0.0006)$
$\log K_c/(\mathrm{m\ s^{-1}})$	$\mathcal{U}(-3, 3)$
$h_c = \sqrt{e}\cos\omega$	$\mathcal{U}(-1, 1)$
$k_c = \sqrt{e}\sin\omega$	$\mathcal{U}(-1, 1)$
Spectrograph Parameters	
γ_i [m s^{-1}]	$\mathcal{U}(-20, 20)$ + median(**rv**)
$\log s_i/(\mathrm{m\ s^{-1}})$	$\mathcal{U}(-5, 5)$

We proceed with modeling our full RV data set with a Keplerian model for each transiting planet, plus a GP activity model for each spectrograph. We use a custom-built `python` package, as described in Cloutier et al. (2021), to sample the joint posterior of our complete RV model that incorporates the affine-invariant MCMC sampler `emcee` (Foreman-Mackey et al. 2013) and the `george` package (Ambikasaran et al. 2015) to evaluate the marginalized likelihood of our GP activity model components. We adopt the model parameter priors reported in Table 2. We recover the median a posteriori GP hyperparameters and construct the predictive GP distributions for each spectrograph. We treat the mean function of each predictive distribution as the best-fit activity model for that spectrograph.

We use this analysis to evaluate the evidence for a second planet. Specifically, we calculate the Perrakis estimator (Perrakis et al. 2014), as used by Díaz et al. (2016), as an importance sampler to estimate the Bayesian model evidences for the one and two-planet RV+GP models. We find that the evidence ratio $\mathcal{Z}_2/\mathcal{Z}_1 = 1202$, which supports the confirmation of the 3.12 day planet in our RV time series (Nelson et al. 2020). We conclude that a two-planet model is heavily favored over a one-planet model when including an explicit activity model in the form of a quasiperiodic GP.

4.5. Rotational Velocities and RVs of LTT 1445BC

We have determined with our MEarth photometry that the 1.4 day rotational modulation we see in the TESS data originates from LTT 1445BC, as discussed in Section 3.1.2. However, we are not able to determine from the photometric time series alone whether the B or C component is the source of that signal. Very-high-resolution spectra of LTT 1445BC might permit the measurement of the rotational velocities of each component, which would allow us to determine the source. We

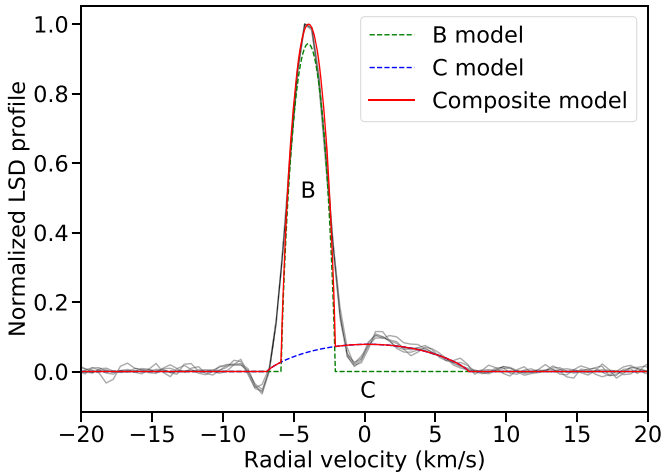

Figure 8. Least-squares deconvolution profiles of LTT 1445B (green dashed line) and C (blue dashed line) from HARPS data (gray lines), which indicate the rotational broadening for each of the B and C components. The solid red line shows the joint fit of the broadened spectra.

noted in Section 3.3.2 that seven of our initial HARPS spectra of LTT 1445 were of the blended BC component. We downloaded these publicly available data and analyzed them using `todcor` (Zucker & Mazeh 1994) and the methods described in Winters et al. (2020) to extract individual RVs and rotational velocities ($v \sin i$) for the B and C components.

We used an observation of Barnard's Star taken UT 2017 September 22 as the template for our analysis. We searched for the nonlinear least-squares maximum likelihood value for three parameters: the flux ratio α and the two values of $v \sin i$. We calculate α, the ratio of the flux of C relative to that of B, to be 0.31 at wavelengths 6760–6836 Å (echelle aperture 71 of the HARPS data), roughly equivalent to filter R_{KC}. While this seems a bit low when compared to the α value of 0.50 we expect from photometry ($\Delta R_{KC} = 0.75 \pm 0.03$ mag; Henry et al. 2006), the angular separation between B and C at the time of these observations is comparable to the HARPS 1″ fiber diameter. Thus, it is reasonable that there is less light from LTT 1445C landing in the fiber.

With this caveat in mind, we measure an average rotational broadening of 7.1 km s^{-1} for LTT 1445C and 1.9 km s^{-1} for LTT 1445B from the six spectra taken in September. These measurements suggest that the 1.4 day rotation period comes from the C component, and the 6.7 day marginal peak we see in the residual periodograms of the TESS and MEarth photometry in Figure 1 is probably the rotation period of the B component. (We note that these results are not completely conclusive, due to $\sin i$ degeneracy. If the 6.7 day photometric period is spurious, then B could be the origin of the 1.4 day period, if we simply have not detected the photometric period of C. However, we view this possibility as unlikely.) Furthermore, we note that, while we have not robustly detected rotational broadening in B, our solutions do slightly prefer some.

As part of our analysis, we measure individual RVs for LTT 1445B and LTT 1445C of -3.98 ± 0.01 km s^{-1} and 0.24 ± 0.20 km s^{-1}. We use the least-squares deconvolution (Donati et al. 1997) to visualize the rotational broadening profiles of LTT 1445B and C in Figure 8.

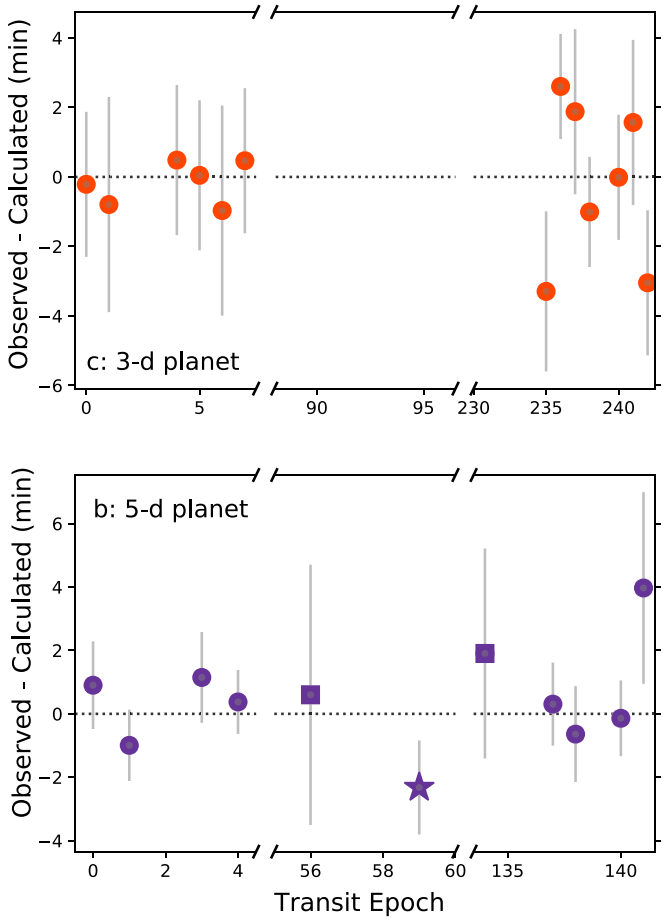

Figure 9. Transit midtimes of the LTT 1445A planets. We show the measured transit midtimes for LTT 1445Ac (orange points, top panel) and for LTT 1445Ab (purple points, bottom panel). The transit midtimes for LTT 1445Ab from TESS, LCO, and MEarth data are noted as filled points, squares, and a star, respectively; transit midtimes for LTT 1445Ac are from TESS data only. As illustrated, the transit times for each planet are consistent with zero (dotted lines), when considering the uncertainties.

4.6. Check of Consistency Across Fits

We performed a number of quality checks to ensure that our results are robust. We investigate three sets of parameters to check for consistency between model fits. We first compare the radius ratios we determine for each of the transit data sets. We then turn to the RV data, and compare both the RV semiamplitude and the eccentricities from different analyses.

We made separate adjustments to the PDCSAP light curves from both sectors of TESS data to correct the excess light from other stars in the optimal aperture. To ensure that we performed this correctly, we compare the results from fitting the transits of LTT 1445Ab from each sector of TESS data and find consistent planet-to-star radius ratios R_p/R_*. From the sector 4 data, we measure the radius ratio to be 0.0465 ± 0.0015, compared to that from sector 31, which is $0.0436^{+0.0015}_{-0.0014}$. We also compare the transit depth measurement results of LTT 1445Ab from our ground-based data to those from our global model. The measured radius ratio of the planet to the host star from ground-based data from MEarth and LCO are 0.0435 ± 0.0021 and $0.049^{+0.004}_{-0.003}$ (68.3% interval), respectively. These are both in agreement with the measured R_p/R_* of $0.0451^{+0.0014}_{-0.0013}$ from our global model. The agreement between all three measurements

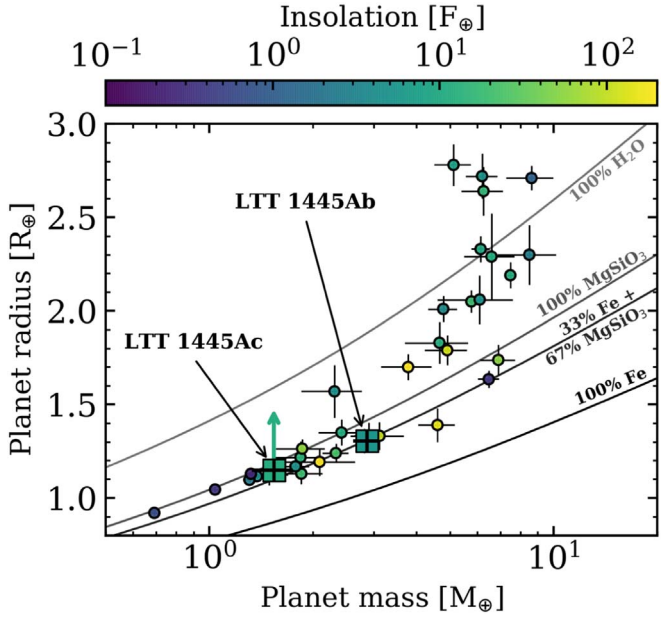

Figure 10. Masses and radii for small planets transiting M dwarfs and with precisely ($\geqslant 3\sigma$) measured masses. The solid curves are illustrative interior structure models of 100% water, 100% magnesium silicate rock, 33% iron plus 67% rock (i.e., Earth-like), and 100% iron from Zeng & Sasselov (2013). LTT 1445Ab and c are depicted by square markers. LTT 1445Ab falls exactly on the composition curve corresponding to the Earth's ratio of iron (and nickel) to a magnesium silicate. Although we measure the mass of LTT 1445Ac, we have deduced only a lower limit on its radius (green arrow), corresponding to the configuration where the transits are not grazing. If indeed they are not grazing, then the radius of LTT 1445Ac would be the minimum value depicted by the square marker here and would lie on the same composition curve as LTT 1445Ab.

of the radius ratio of LTT 1445Ab indicates that we correctly adjusted the TESS dilution factor. We are not able to perform a radius ratio comparison for LTT 1445Ac because we do not yet have an independent ground-based detection of it.

We compare the results from our global model to the results from our modeling of the RVs with a GP. The measured RV semiamplitudes from the RV+GP model for planets c and b are 1.49 ± 0.17 m s^{-1} and 2.28 ± 0.17 m s^{-1}, while they are 1.67 ± 0.20 m s^{-1}, and 2.60 ± 0.21 m s^{-1} from our global model for planets c and b, respectively. All measurements are in agreement.

From the RV+GP model, the 95% confidence intervals for the eccentricities of the orbits of c and b are <0.165 and <0.089, respectively. These are in agreement with the results from our global model, which are <0.223 and <0.110, respectively.

Because the results from our RV+GP model and our global ExoFASTv2 model are in agreement, we determined that the inclusion of a GP to model any periodic stellar variability in our RVs is unnecessary. Thus, we adopt the median values from our global ExoFASTv2 model as our preferred results.

4.7. Search for Transit Timing Variations

Multiplanet systems sometimes exhibit transit timing variations (TTVs; Agol et al. 2005; Holman & Murray 2005), and we might expect them in the LTT 1445 system because the orbital periods of the two planets are not too dissimilar. Using the case of two planets not in resonance on circular orbits from Agol et al. (2005), we calculate that TTVs for the LTT 1445A planets are expected to be on the order of 1 min for each planet. We utilized ExoFASTv2's TTV capability to search for variations in each planet's transit midtimes, but did not detect any. We ran 213 chains for 3000 steps, thinned by 300, for a total number of 191.7 million simulations. For LTT 1445Ac, the shallow transit depth, grazing geometry, and low S/N of the light curves thwarted our efforts to reach a Gelman–Rubin value of less than 1.05 for the TTV parameters. Therefore, for this TTV analysis only, we adopt the criterion of convergence at a Gelman–Rubin value less than 1.1 (Gelman et al. 2004). We omit transit 239 from our TTV analysis because it has two solutions, and provide the midtransit times for each planet's transit from all of the time series photometry in Table 4. We show in Figure 9 that the transit midtimes of both planets are consistent with a linear solution when considering the uncertainties.

5. Discussion and Conclusions

We have measured the mass and radius of LTT 1445Ab to a precision of 9% and 5%, respectively. These precise mass and radius measurements permit the investigation of the planetary core mass fraction (CMF), which provides a probe for the planetary composition. Using the semiempirical relation from Zeng et al. (2016), we calculate a CMF of 0.425 ± 0.283 for LTT 1445Ab. This is illustrated in the radius versus mass diagram in Figure 10, which includes composition curves from Zeng & Sasselov (2013). The planet falls squarely on the rocky compositional curve of 33% iron plus 67% magnesium silicate. In the near future, we hope to determine the abundances of key elements in the stellar photosphere, and see if they match the ratios we have inferred for the planet for its bulk composition.

We have detected a second planet transiting LTT 1445A. The presence of additional planets orbiting LTT 1445A is not surprising, given the previously known existence of LTT 1445Ab (W19) and the recent result that 90^{+5}_{-21}% of mid-M dwarfs host multiple planets less massive than 10 $M_\oplus$ and with orbital periods less than 50 days (Cloutier et al. 2021). LTT 1445A joins the growing list of mid-M dwarf systems in which additional planets have been revealed via follow-up observations of the original discovered planet. Some examples include GJ 357 cd (Luque et al. 2019), GJ 1132c (Bonfils et al. 2018), GJ 3473c (Kemmer et al. 2020), and LHS 1140c (Ment et al. 2019).

While we have measured the mass of LTT 1445Ac to a precision of 13%, the TESS data do not permit us to determine if all four points of contact are present in the transit curve of LTT 1445Ac, and hence whether the planetary transits are grazing. While the measured depth provides a minimum value for the radius of LTT 1445Ac, a grazing configuration allows acceptable solutions of arbitrarily large radii for the transiting object. If we impose a prior based on the mass–radius relation of Chen & Kipping (2017), then we find an acceptable, nongrazing fit to the light curve, and the resulting planet radius is $1.147^{+0.055}_{-0.053}\,R_\oplus$. This would correspond to a CMF of 0.235 ± 0.297, again consistent with the telluric value. Ultimately this question requires a more precise light curve, and we eagerly await the observations scheduled with HST (HST-GO-16503; PI: J. Winters).

Intriguingly, our results indicate that the two planets have circular (or low-eccentricity) orbits that are misaligned by at least $-2.25^{+0.28}_{-0.29}$ degrees (as inferred from the posterior of the global model fit). This value is a lower limit for several reasons.

Table 3
ExoFASTv2 Median Values and 68% Confidence Intervals for LTT 1445Ac & LTT 1445Ab

Parameter	Units	Values	
Host Star Parameters:		LTT 1445A	
M_*…	Stellar mass ($M_\odot$)	0.257 ± 0.014	
R_*…	Stellar radius ($R_\odot$)	$0.265^{+0.011}_{-0.010}$	
$T_{\rm eff}$…	Stellar effective temp. (K)	3340 ± 150	
[Fe/H]…	Stellar metallicity	-0.34 ± 0.09	
$\dot{\gamma}$…	RV slope[a] (m s^{-1} day^{-1})	$-0.0081^{+0.0026}_{-0.0029}$	
Planetary Parameters:		LTT 1445Ac	LTT 1445Ab
P…	Period (days)…	$3.1239035^{+0.0000034}_{-0.0000036}$	$5.3587657^{+0.0000043}_{-0.0000042}$
R_P…	Radius[f] ($R_{\rm E}$)…	$1.147^{+0.055}_{-0.054}$	$1.305^{+0.066}_{-0.061}$
M_P…	Mass ($M_{\rm E}$)…	$1.54^{+0.20}_{-0.19}$	$2.87^{+0.26}_{-0.25}$
T_C…	Time of conjunction[b] ($\rm BJD_{TDB}$)…	$2458412.58159^{+0.00059}_{-0.00057}$	$2458412.70851^{+0.00040}_{-0.00039}$
T_T…	Time of min. proj. sep.[c] ($\rm BJD_{TDB}$)…	$2458412.58156^{+0.00059}_{-0.00057}$	$2458412.70851^{+0.00040}_{-0.00039}$
i…	Inclination[f] (Degrees)…	$87.43^{+0.18}_{-0.29}$	$89.68^{+0.22}_{-0.29}$
e…	Eccentricity[d] …	<0.223	<0.110
K…	RV semiamplitude (m s^{-1})…	$1.67^{+0.21}_{-0.20}$	2.60 ± 0.21
δ…	Transit depth (fraction)…	$0.00157^{+0.00015}_{-0.00014}$	0.00203 ± 0.00012
T_{14}…	Total transit duration (days)…	0.0201 ± 0.0011	$0.05697^{+0.00071}_{-0.00068}$
a…	Semimajor axis (au)…	$0.02661^{+0.00047}_{-0.00049}$	$0.03813^{+0.00068}_{-0.00070}$
R_P/R_*…	Radius of planet in stellar radii[f] …	$0.0396^{+0.0018}_{-0.0017}$	$0.0451^{+0.0014}_{-0.0013}$
a/R_*…	Semimajor axis in stellar radii …	$21.56^{+0.78}_{-0.82}$	$30.9^{+1.1}_{-1.2}$
b…	Transit impact parameter[f] …	$0.937^{+0.012}_{-0.016}$	$0.17^{+0.15}_{-0.12}$
b_S…	Eclipse impact parameter[f] …	$0.977^{+0.20}_{-0.089}$	$0.17^{+0.14}_{-0.12}$
ρ_P…	Density[f] (g cm^{-3})…	$5.57^{+0.68}_{-0.60}$	$7.1^{+1.2}_{-1.1}$
$log(g_P)$…	Surface gravity[f] …	$3.057^{+0.042}_{-0.043}$	$3.217^{+0.050}_{-0.053}$
$\langle F \rangle$…	Incident flux (10^9 erg s^{-1} cm^{-2})…	$0.0149^{+0.0032}_{-0.0027}$	$0.0073^{+0.0016}_{-0.0013}$
$T_{\rm eq}$…	Equilibrium temperature[e](K)…	508 ± 25	424 ± 21
Wavelength Parameters:		TESS	
u_1…	Linear limb-darkening coeff …	$0.156^{+0.079}_{-0.076}$	
u_2…	Quadratic limb-darkening coeff …	0.396 ± 0.093	
A_D…	Dilution from neighboring stars …	$-0.012^{+0.048}_{-0.049}$	
Spectrograph Parameters:		Relative RV Offset[a] (m s^{-1})	RV Jitter (m s^{-1})
ESPRESSO …		$-5460.28^{+0.50}_{-0.53}$	$0.96^{+0.23}_{-0.17}$
HARPS (2019) …		$-5458.7^{+1.4}_{-1.5}$	$1.9^{+1.7}_{-1.0}$
HARPS (2020) …		$-5453.51^{+0.63}_{-0.64}$	$2.30^{+0.45}_{-0.38}$
HIRES …		-1.75 ± 0.45	$2.29^{+0.45}_{-0.39}$
MAROON-X (2019) …		$-0.14^{+0.58}_{-0.53}$	$1.16^{+0.74}_{-0.49}$
MAROON-X (2020) …		$1.84^{+0.78}_{-0.72}$	$0.93^{+0.29}_{-0.22}$
PFS …		$0.41^{+0.58}_{-0.54}$	$1.87^{+0.60}_{-0.43}$
TESS Transit Parameters:		Added Variance σ^2	Baseline flux F_0
2018…		$0.000000170^{+0.000000039}_{-0.000000036}$	0.999954 ± 0.000031
2020…		$-0.000000009^{+0.000000038}_{-0.000000036}$	1.000084 ± 0.000030

Notes. See Table 3 in Eastman et al. (2019) for a detailed description of all parameters.
[a] Reference epoch = 2458868.217394.
[b] Time of conjunction is commonly reported as the "transit time."
[c] Time of minimum projected separation is a more correct "transit time."
[d] $2-\sigma$ (95%) upper limits.
[e] Assumes no albedo and perfect redistribution.
[f] The value for planet c was derived using the measured mass, the lower limit on the radius from the light curve, and Chen & Kipping (2017) exoplanet mass–radius relation to estimate the planetary radius.

First, it results from the inclusion of the mass–radius relation of Chen & Kipping (2017), which results in nongrazing transits. Grazing transits by a larger planet would result in an even larger misalignment. Second, even if this solution is correct and the transits are not grazing, we observe only a projection onto the line of sight of the true misalignment between the planetary orbits. Third, there is an (i, $180-i$) degeneracy and if the two orbits are on opposite sides of the central crossing, the mutual

Table 4
Median Values and 68% Confidence Interval for Planet Transit Midtimes

Transit	Planet	Epoch	T_T
TESS UT 2018-10-21 (TESS)	c	0	$2458412.5815^{+0.0014}_{-0.0015}$
TESS UT 2018-10-24 (TESS)	c	1	$2458415.7050^{+0.0023}_{-0.0020}$
TESS UT 2018-11-02 (TESS)	c	4	2458425.0776 ± 0.0015
TESS UT 2018-11-05 (TESS)	c	5	$2458428.2012^{+0.0014}_{-0.0016}$
TESS UT 2018-11-08 (TESS)	c	6	$2458431.3244^{+0.0024}_{-0.0018}$
TESS UT 2018-11-11 (TESS)	c	7	$2458434.4493^{+0.0015}_{-0.0014}$
TESS UT 2020-10-24 (TESS)	c	235	$2459146.6968^{+0.0017}_{-0.0015}$
TESS UT 2020-10-27 (TESS)	c	236	$2459149.8248^{+0.0010}_{-0.0011}$
TESS UT 2020-10-30 (TESS)	c	237	$2459152.9482^{+0.0018}_{-0.0015}$
TESS UT 2020-11-02 (TESS)	c	238	2459156.0701 ± 0.0011
TESS UT 2020-11-08 (TESS)	c	240	$2459162.3186^{+0.0013}_{-0.0012}$
TESS UT 2020-11-11 (TESS)	c	241	$2459165.4436^{+0.0017}_{-0.0016}$
TESS UT 2020-11-15 (TESS)	c	242	$2459168.5643^{+0.0015}_{-0.0014}$
TESS UT 2018-10-21 (TESS)	b	0	$2458412.70898^{+0.00099}_{-0.00093}$
TESS UT 2018-10-26 (TESS)	b	1	$2458418.06643^{+0.00080}_{-0.00076}$
TESS UT 2018-11-06 (TESS)	b	3	$2458428.78545^{+0.00099}_{-0.0010}$
TESS UT 2018-11-11 (TESS)	b	4	$2458434.14368^{+0.00075}_{-0.00065}$
LCO UT 2019-08-16 (z')	b	56	$2458712.7997^{+0.0030}_{-0.0027}$
MEarth UT 2019-09-02 (TESS)	b	59	$2458728.87397^{+0.00096}_{-0.0011}$
LCO UT 2020-10-08 (z')	b	134	$2459130.7844^{+0.0018}_{-0.0028}$
TESS UT 2020-10-24 (TESS)	b	137	$2459146.85959^{+0.00092}_{-0.00090}$
TESS UT 2020-10-29 (TESS)	b	138	$2459152.21770^{+0.00080}_{-0.0013}$
TESS UT 2020-11-09 (TESS)	b	140	$2459162.93558^{+0.00089}_{-0.00077}$
TESS UT 2020-11-14 (TESS)	b	141	$2459168.2972^{+0.0019}_{-0.0023}$

inclination would be $-2.91^{+0.34}_{-0.45}$ degrees, larger than the value presented above. For reference, the mutual inclination of the orbits of Venus and the Earth is 3.4 degrees.

We confirmed that the 1.4 day rotational modulation seen in the TESS data originates from LTT 1445BC. We have calculated the $v \sin i$ and RV values for LTT 1445B and C individually and find that the 1.4 day signal is likely the rotation period of LTT 1445C, while the less statistically significant 6.7 day signal may be the rotation period of LTT 1445B. From the activity and mass of LTT 1445A, we expect its rotation period to be 85 ± 22 days, based on the empirical relation in Newton et al. (2017). We have not yet detected the rotation period with MEarth, but our observations are ongoing. If our estimated rotation rates are correct, it implies that this triple star system is in a special evolutionary state, where A has spun down, B is in the process of spinning down, and C has not yet begun to spin down. LTT 1445 could be an important benchmark system for rotational evolution because it directly samples the mass dependence of the rapid spin-down phase discussed in the context of mid-to-late field M dwarfs by Newton et al. (2017). Intriguingly, the dynamical masses of the stars B and C can eventually be estimated directly, although this may take some time given the moderately long orbital period of 36.2 ± 5.3 yr (W19).

LTT 1445 is the second-closest known transiting exoplanet system, and the closest one with an M dwarf host star. Due to the efforts of MEarth (Nutzman & Charbonneau 2008; Irwin et al. 2015), TRAPPIST (Gillon et al. 2016, 2017), and TESS (Ricker et al. 2015), there are currently 10 systems among the M dwarfs within 15 pc with masses $\leqslant 0.35\ M/M_{\odot}$ that are known to host transiting planets: GJ 1214b (Charbonneau et al. 2009), GJ 1132bc (Berta-Thompson et al. 2015; Bonfils et al. 2018), TRAPPIST-1 (Gillon et al. 2016, 2017; Grimm et al. 2018), LHS 1140bc (Dittmann et al. 2017; Ment et al. 2019), LHS 3844b (Vanderspek et al. 2019), LTT 1445Abc (W19; this work), L 98-59bcd (Kostov et al. 2019; Cloutier et al. 2019), GJ 357b (Luque et al. 2019), 2MA 0505-4756b (TOI-540b; Ment et al. 2021), and GJ 486b (Trifonov et al. 2021). Although challenging, these planets are among the very best available for near-future studies of their atmospheres. Kempton et al. (2018) provide empirical relations that allow for a quantitative comparison of the S/N of spectra acquired with the James Webb Space Telescope, based on the stellar and planetary properties. For LTT 1445Ab, we calculate a transmission spectroscopy metric (TSM) of 30 for LTT 1445Ab and an emission spectroscopy metric (ESM) of 5.7. If LTT 1445Ac is indeed terrestrial with the values listed in Table 3, then it would have an even higher TSM of 46 and an ESM of 8.7. For reference, Kempton et al. (2018) recommend minimum TSM and ESM values of 10 and 7.5, respectively, for planets that should be prioritized for future atmospheric studies. Furthermore, the proximity of LTT 1445A makes it a good candidate for stellar wind and mass-loss-rate measurements, as recently detailed in Wood et al. (2021), to determine their effect on the planetary atmospheres, should those be present.

W19 noted that, given the transit probability and number of nearby mid-to-late M dwarfs, TESS might find one more planet that is as accessible to follow-up study as LTT 1445Ab. LTT 1445Ac would appear to satisfy that criterion. As TESS has observed roughly 80% of the sky, the LTT 1445 system may remain the closest small star with transiting exoplanets. Then again, perhaps the remaining 20% of the sky will hold some as-yet undiscovered jewels.

We thank the referee for a thoughtful and prompt review that improved the manuscript. This work is made possible by a

grant from the John Templeton Foundation. The opinions expressed in this publication are those of the authors and do not necessarily reflect the views of the John Templeton Foundation. The MEarth Team gratefully acknowledges funding from the David and Lucile Packard Fellowship for Science and Engineering (awarded to D.C.). This material is based upon work supported by the National Science Foundation under grant AST-1616624, and work supported by the National Aeronautics and Space Administration under Grant No. 80NSSC18K0476 issued through the XRP Program.

This paper includes data collected by the TESS mission that are publicly available from the Mikulski Archive for Space Telescopes (MAST). We acknowledge the use of public TESS data from pipelines at the TESS Science Office and at the TESS Science Processing Operations Center. This research has made use of the Exoplanet Follow-up Observation Program website, which is operated by the California Institute of Technology, under contract with the National Aeronautics and Space Administration under the Exoplanet Exploration Program. Resources supporting this work were provided by the NASA High-end Computing (HEC) Program through the NASA Advanced Supercomputing (NAS) Division at Ames Research Center for the production of the SPOC data products. Funding for the TESS mission is provided by the NASA's Science Mission Directorate.

This work makes use of observations from the LCOGT network. Part of the LCOGT telescope time was granted by NOIRLab through the Mid-scale Innovations Program (MSIP). MSIP is funded by NSF. This work was enabled by observations made from the Gemini-North telescope, located within the Maunakea Science Reserve and adjacent to the summit of Maunakea. The authors wish to recognize and acknowledge the very significant cultural role and reverence that the summit of Maunakea has always had within the indigenous Hawaiian community. We are grateful for the privilege of observing the Universe from a place that is unique in both its astronomical quality and its cultural significance. The international Gemini Observatory, a program of NSF's NOIRLab, is managed by the Association of Universities for Research in Astronomy (AURA) under a cooperative agreement with the National Science Foundation. on behalf of the Gemini Observatory partnership: the National Science Foundation (United States), National Research Council (Canada), Agencia Nacional de Investigación y Desarrollo (Chile), Ministerio de Ciencia, Tecnología e Innovación (Argentina), Ministério da Ciência, Tecnologia, Inovações e Comunicações (Brazil), and Korea Astronomy and Space Science Institute (Republic of Korea). The MAROON-X spectrograph was funded by the David and Lucile Packard Foundation, the Heising–Simons Foundation, the Gemini Observatory, and the University of Chicago. This paper includes data gathered with the 6.5 meter Magellan Telescopes located at Las Campanas Observatory, Chile. Some of the data presented herein were obtained at the W. M. Keck Observatory, which is operated as a scientific partnership among the California Institute of Technology, the University of California and the National Aeronautics and Space Administration. The observatory was made possible by the generous financial support of the W. M. Keck Foundation.

This work has made use of data from the European Space Agency (ESA) mission Gaia (https://www.cosmos.esa.int/gaia), processed by the Gaia Data Processing and Analysis Consortium (DPAC; https://www.cosmos.esa.int/web/gaia/dpac/consortium). Funding for the DPAC has been provided by national institutions, in particular the institutions participating in the Gaia Multilateral Agreement. Data products from the Two Micron All Sky Survey, which is a joint project of the University of Massachusetts and the Infrared Processing and Analysis Center/California Institute of Technology, funded by NASA and the NSF have been used in this publication. This work has made use of the Washington Double Star Catalog maintained at the U.S. Naval Observatory. This work has made use of the Smithsonian Astrophysical Observatory/NASA Astrophysics Data System.

R.C. acknowledges support from the Banting Postdoctoral Fellowship program, administered by the Government of Canada. N.A.-D. acknowledges the support of FONDECYT project 3180063. J.M.A.M. is supported by the NSF Graduate Research Fellowship, grant No. DGE-1842400. J.M.A.M. also acknowledges the LSSTC Data Science Fellowship Program, which is funded by LSSTC, NSF Cybertraining Grant No. 1829740, the Brinson Foundation, and the Moore Foundation; his participation in the program has benefited this work. D.H. acknowledges support from the Alfred P. Sloan Foundation, NASA (80NSSC21K0652), and the National Science Foundation (AST-1717000). K.H. acknowledges support from STFC grant ST/R000824/1. T.F. acknowledges support from the University of California President's Postdoctoral Fellowship Program. P.D. acknowledges support from a National Science Foundation Astronomy and Astrophysics Postdoctoral Fellowship under award AST-1903811.

Facilities: TESS, MEarth, LCOGT, ESO:3.6 m (HARPS), Gemini:Gillett (MAROON-X), Keck (HIRES), Magellan: Clay (PFS), VLT (ESPRESSO).

Software: `AstroImageJ` (Collins et al. 2017), `astropy` (Astropy Collaboration et al. 2013, 2018), `barycorrpy` (Kanodia & Wright 2018), `celerite` (Foreman-Mackey et al. 2017), `ExoFASTv2` (Eastman et al. 2013; Eastman 2017), `exoplanet` (Foreman-Mackey et al. 2019), `george` (Ambikasaran et al. 2015), IDL, IRAF, `LcTools II` (Schmitt & Vanderburg 2021), `PYMC3` (Salvatier et al. 2016), `python`, `serval` (Zechmeister et al. 2018), `starry` (Luger et al. 2019), `TAPIR` (Jensen 2013), Time Utilities (Eastman et al. 2010), `todcor` (Zucker & Mazeh 1994).

ORCID iDs

Jennifer G. Winters https://orcid.org/0000-0001-6031-9513
Ryan Cloutier https://orcid.org/0000-0001-5383-9393
Amber A. Medina https://orcid.org/0000-0001-8726-3134
David Charbonneau https://orcid.org/0000-0002-9003-484X
Nicola Astudillo-Defru https://orcid.org/0000-0002-8462-515X
Andrew W. Howard https://orcid.org/0000-0001-8638-0320
Howard Isaacson https://orcid.org/0000-0002-0531-1073
Jacob L. Bean https://orcid.org/0000-0003-4733-6532
Andreas Seifahrt https://orcid.org/0000-0003-4526-3747
Jason D. Eastman https://orcid.org/0000-0003-3773-5142
Joseph D. Twicken https://orcid.org/0000-0002-6778-7552
Karen A. Collins https://orcid.org/0000-0001-6588-9574
Eric L. N. Jensen https://orcid.org/0000-0002-4625-7333
Samuel N. Quinn https://orcid.org/0000-0002-8964-8377
Matthew J. Payne https://orcid.org/0000-0001-5133-6303
Martti H. Kristiansen https://orcid.org/0000-0002-2607-138X

Andrew Vanderburg https://orcid.org/0000-0001-7246-5438
Mathias Zechmeister https://orcid.org/0000-0002-6532-4378
Lauren M. Weiss https://orcid.org/0000-0002-3725-3058
Sharon Xuesong Wang https://orcid.org/0000-0002-6937-9034
Gavin Wang https://orcid.org/0000-0003-3092-4418
Stéphane Udry https://orcid.org/0000-0001-7576-6236
Ivan A. Terentev https://orcid.org/0000-0002-0654-4442
Julian Stürmer https://orcid.org/0000-0002-4410-4712
Gudmundur Stefánsson https://orcid.org/0000-0001-7409-5688
Avi Shporer https://orcid.org/0000-0002-1836-3120
Stephen Shectman https://orcid.org/0000-0002-8681-6136
Ramotholo Sefako https://orcid.org/0000-0003-3904-6754
Hans Martin Schwengeler https://orcid.org/0000-0002-1637-2189
Richard P. Schwarz https://orcid.org/0000-0001-8227-1020
Nicholas Scarsdale https://orcid.org/0000-0003-3623-7280
Ryan A. Rubenzahl https://orcid.org/0000-0003-3856-3143
Arpita Roy https://orcid.org/0000-0001-8127-5775
Paul Robertson https://orcid.org/0000-0003-0149-9678
Erik A. Petigura https://orcid.org/0000-0003-0967-2893
Joseph M. Akana Murphy https://orcid.org/0000-0001-8898-8284
Felipe Murgas https://orcid.org/0000-0001-9087-1245
Teo Močnik https://orcid.org/0000-0003-4603-556X
Benjamin T. Montet https://orcid.org/0000-0001-7516-8308
Ronald Mennickent https://orcid.org/0000-0002-6245-0264
Andrew W. Mayo https://orcid.org/0000-0002-7216-2135
Bob Massey https://orcid.org/0000-0001-8879-7138
Jack Lubin https://orcid.org/0000-0001-8342-7736
Pablo Lewin https://orcid.org/0000-0003-0828-6368
David Kasper https://orcid.org/0000-0003-0534-6388
Stephen R. Kane https://orcid.org/0000-0002-7084-0529
Jon M. Jenkins https://orcid.org/0000-0002-4715-9460
Daniel Huber https://orcid.org/0000-0001-8832-4488
Keith Horne https://orcid.org/0000-0003-1728-0304
Michelle L. Hill https://orcid.org/0000-0002-0139-4756
Paula Gorrini https://orcid.org/0000-0002-6394-6544
Steven Giacalone https://orcid.org/0000-0002-8965-3969
Benjamin Fulton https://orcid.org/0000-0003-3504-5316
Thierry Forveille https://orcid.org/0000-0003-0536-4607
Tara Fetherolf https://orcid.org/0000-0002-3551-279X
Courtney Dressing https://orcid.org/0000-0001-8189-0233
Rodrigo F. Díaz https://orcid.org/0000-0001-9289-5160
Xavier Delfosse https://orcid.org/0000-0001-5099-7978
Paul A. Dalba https://orcid.org/0000-0002-4297-5506
Fei Dai https://orcid.org/0000-0002-8958-0683
Jeffrey D. Crane https://orcid.org/0000-0002-5226-787X
Dennis M. Conti https://orcid.org/0000-0003-2239-0567
Kevin I. Collins https://orcid.org/0000-0003-2781-3207
Ashley Chontos https://orcid.org/0000-0003-1125-2564
R. Paul Butler https://orcid.org/0000-0003-1305-3761
Peyton Brown https://orcid.org/0000-0002-3481-9052
Aida Behmard https://orcid.org/0000-0003-0012-9093
Corey Beard https://orcid.org/0000-0001-7708-2364
Natalie M. Batalha https://orcid.org/0000-0002-7030-9519
Jose-Manuel Almenara https://orcid.org/0000-0003-3208-9815

References

Agol, E., Steffen, J., Sari, R., & Clarkson, W. 2005, MNRAS, 359, 567
Akaike, H. 1974, ITAC, 19, 716
Ambikasaran, S., Foreman-Mackey, D., Greengard, L., Hogg, D. W., & O'Neil, M. 2015, ITPAM, 38, 252
Angus, R., Morton, T., Aigrain, S., Foreman-Mackey, D., & Rajpaul, V. 2018, MNRAS, 474, 2094
Astropy Collaboration, Robitaille, T. P., Tollerud, E. J., et al. 2013, A&A, 558, A33
Astropy Collaboration, Price-Whelan, A. M., Sipőcz, B. M., et al. 2018, AJ, 156, 123
Astudillo-Defru, N., Delfosse, X., Bonfils, X., et al. 2017, A&A, 600, A13
Astudillo-Defru, N., Bonfils, X., Delfosse, X., et al. 2015, A&A, 575, A119
Bean, J. L., Seifahrt, A., Hartman, H., et al. 2010, ApJ, 713, 410
Benedict, G. F., Henry, T. J., Franz, O. G., et al. 2016, AJ, 152, 141
Berta-Thompson, Z. K., Irwin, J., Charbonneau, D., et al. 2015, Natur, 527, 204
Bonfils, X., Almenara, J. M., Cloutier, R., et al. 2018, A&A, 618, A142
Bouchy, F., Pepe, F., & Queloz, D. 2001, A&A, 374, 733
Boyajian, T. S., von Braun, K., van Belle, G., et al. 2012, ApJ, 757, 112
Brown, T. M., Baliber, N., Bianco, F. B., et al. 2013, PASP, 125, 1031
Butler, R. P., Marcy, G. W., Williams, E., et al. 1996, PASP, 108, 500
Charbonneau, D., Berta, Z. K., Irwin, J., et al. 2009, Natur, 462, 891
Chen, J., & Kipping, D. 2017, ApJ, 834, 17
Claret, A. 2017, A&A, 600, A30
Cloutier, R., Astudillo-Defru, N., Doyon, R., et al. 2017, A&A, 608, A35
Cloutier, R., Astudillo-Defru, N., Bonfils, X., et al. 2019, A&A, 629, A111
Cloutier, R., Eastman, J. D., Rodriguez, J. E., et al. 2020a, AJ, 160, 3
Cloutier, R., Rodriguez, J. E., Irwin, J., et al. 2020b, AJ, 160, 22
Cloutier, R., Charbonneau, D., Stassun, K. G., et al. 2021, AJ, 162, 79
Collins, K. A., Kielkopf, J. F., Stassun, K. G., & Hessman, F. V. 2017, AJ, 153, 77
Crane, J. D., Shectman, S. A., & Butler, R. P. 2006, Proc. SPIE, 6269, 626931
Crane, J. D., Shectman, S. A., Butler, R. P., et al. 2010, Proc. SPIE, 7735, 773553
Crane, J. D., Shectman, S. A., Butler, R. P., Thompson, I. B., & Burley, G. S. 2008, Proc. SPIE, 7014, 701479
Díaz, R. F., Ségransan, D., Udry, S., et al. 2016, A&A, 585, A134
Dittmann, J. A., Irwin, J. M., Charbonneau, D., et al. 2017, Natur, 544, 333
Donati, J.-F., Semel, M., Carter, B. D., Rees, D. E., & Collier Cameron, A. 1997, MNRAS, 291, 658
Eastman, J. 2017, EXOFASTv2: Generalized publication-quality exoplanet modeling code, Astrophysics Source Code Library, ascl:1710.003
Eastman, J., Gaudi, B. S., & Agol, E. 2013, PASP, 125, 83
Eastman, J., Siverd, R., & Gaudi, B. S. 2010, PASP, 122, 935
Eastman, J. D., Rodriguez, J. E., Agol, E., et al. 2019, arXiv:1907.09480
Foreman-Mackey, D., Agol, E., Ambikasaran, S., & Angus, R. 2017, AJ, 154, 220
Foreman-Mackey, D., Barentsen, G., & Barclay, T. 2019, dfm/exoplanet: exoplanet v0.1.4, https://doi.org/10.5281/zenodo.2561395
Foreman-Mackey, D., Hogg, D. W., Lang, D., & Goodman, J. 2013, PASP, 125, 306
Gaia Collaboration, Prusti, T., de Bruijne, J. H. J., et al. 2016, A&A, 595, A1
Gelman, A., Carlin, J. B., Stern, H. S., & Rubin, D. B. 2004, Bayesian Data Analysis (2nd edn; Boca Raton, FL: CRC Press)
Gelman, A., & Rubin, D. B. 1992, StaSc, 7, 457
Gillon, M., Jehin, E., Lederer, S. M., et al. 2016, Natur, 533, 221
Gillon, M., Demory, B.-O., Van Grootel, V., et al. 2017, NatAs, 1, 0056
Grimm, S. L., Demory, B.-O., Gillon, M., et al. 2018, A&A, 613, A68
Harrington, R. S. 1972, CeMec, 6, 322
Haywood, R. D., Collier Cameron, A., Queloz, D., et al. 2014, MNRAS, 443, 2517
Henry, T. J., Jao, W.-C., Subasavage, J. P., et al. 2006, AJ, 132, 2360
Henry, T. J., Jao, W.-C., Winters, J. G., et al. 2018, AJ, 155, 265
Holman, M. J., & Murray, N. W. 2005, Sci, 307, 1288
Howard, A. W., Johnson, J. A., Marcy, G. W., et al. 2010, ApJ, 721, 1467
Irwin, J. M., Berta-Thompson, Z. K., Charbonneau, D., et al. 2015, in Cambridge Workshop on Cool Stars, Stellar Systems, and the Sun, 18, 18th Cambridge Workshop on Cool Stars, Stellar Systems, and the Sun, ed. G. T. van Belle & H. C. Harris (Cambridge: Cambridge Univ. Press), 767
Jenkins, J. M., Caldwell, D. A., & Borucki, W. J. 2002, ApJ, 564, 495
Jenkins, J. M., Caldwell, D. A., Chandrasekaran, H., et al. 2010, ApJ, 713, L87
Jenkins, J. M., Twicken, J. D., Batalha, N. M., et al. 2015, AJ, 150, 56
Jenkins, J. M., Twicken, J. D., McCauliff, S., et al. 2016, Proc. SPIE, 9913, 99133E

Jensen, E. 2013, Tapir: A web interface for transit/eclipse observability, Astrophysics Source Code Library, ascl:1306.007
Kanodia, S., & Wright, J. 2018, RNAAS, 2, 4
Kemmer, J., Stock, S., Kossakowski, D., et al. 2020, A&A, 642, A236
Kempton, E. M. R., Bean, J. L., Louie, D. R., et al. 2018, PASP, 130, 114401
Kostov, V. B., Schlieder, J. E., Barclay, T., et al. 2019, AJ, 158, 32
Li, J., Tenenbaum, P., Twicken, J. D., et al. 2019, PASP, 131, 024506
Lindegren, L., Klioner, S. A., Hernández, J., et al. 2021, A&A, 649, A2
Luger, R., Agol, E., Foreman-Mackey, D., et al. 2018, STARRY: Analytic computation of occultation light curves, Astrophysics Source Code Library, ascl:1810.005
Luger, R., Agol, E., Foreman-Mackey, D., et al. 2019, AJ, 157, 64
Luque, R., Pallé, E., Kossakowski, D., et al. 2019, A&A, 628, A39
Luyten, W. J. 1957, A catalogue of 9867 stars in the Southern Hemisphere with proper motions exceeding 0.”2 annually
Luyten, W. J. 1980, NLTT Catalogue, Vol. 3 (Minneapolis, MN: Univ. of Minnesota)
Mann, A. W., Feiden, G. A., Gaidos, E., Boyajian, T., & von Braun, K. 2015, ApJ, 804, 64
Mason, B. D., Wycoff, G. L., Hartkopf, W. I., Douglass, G. G., & Worley, C. E. 2009, yCat, B, wds
Mayor, M., Pepe, F., Queloz, D., et al. 2003, Msngr, 114, 20
McCully, C., Volgenau, N. H., Harbeck, D.-R., et al. 2018, Proc. SPIE, 10707, 107070K
Medina, A. A., Winters, J. G., Irwin, J. M., & Charbonneau, D. 2020, ApJ, 905, 107
Ment, K., Dittmann, J. A., Astudillo-Defru, N., et al. 2019, AJ, 157, 32
Ment, K., Irwin, J., Charbonneau, D., et al. 2021, AJ, 161, 23
Meunier, N., Desort, M., & Lagrange, A. M. 2010, A&A, 512, A39
Motalebi, F., Udry, S., Gillon, M., et al. 2015, A&A, 584, A72
Muirhead, P. S., Dressing, C. D., Mann, A. W., et al. 2018, AJ, 155, 180
Nelson, B. E., Ford, E. B., Buchner, J., et al. 2020, AJ, 159, 73
Neves, V., Bonfils, X., Santos, N. C., et al. 2014, A&A, 568, A121
Newton, E. R., Irwin, J., Charbonneau, D., et al. 2017, ApJ, 834, 85
Newton, E. R., Irwin, J., Charbonneau, D., et al. 2016, ApJ, 821, 93
Nutzman, P., & Charbonneau, D. 2008, PASP, 120, 317
Pecaut, M. J., & Mamajek, E. E. 2013, ApJS, 208, 9
Pepe, F., Cristiani, S., Rebolo, R., et al. 2021, A&A, 645, A96
Perrakis, K., Ntzoufras, I., & Tsionas, E. G. 2014, CSDA, 77, 54
Rajpaul, V., Aigrain, S., Osborne, M. A., Reece, S., & Roberts, S. 2015, MNRAS, 452, 2269
Ricker, G. R., Winn, J. N., Vanderspek, R., et al. 2015, JATIS, 1, 014003
Rodriguez, J. E., Becker, J. C., Eastman, J. D., et al. 2018, AJ, 156, 245
Salvatier, J., Wiecki, T. V., & Fonnesbeck, C. 2016, PeerJ Comp. Sci., 2, e55
Schmitt, A., & Vanderburg, A. 2021, arXiv:2103.10285
Schwarz, G. 1978, AnSta, 6, 461
Seifahrt, A., Bean, J. L., Stürmer, J., et al. 2016, Proc. SPIE, 9908, 990818
Seifahrt, A., Stürmer, J., Bean, J. L., & Schwab, C. 2018, Proc. SPIE, 10702, 107026D
Seifahrt, A., Bean, J. L., Stürmer, J., et al. 2020, Proc. SPIE, 11447, 114471F
Smith, J. C., Stumpe, M. C., Van Cleve, J. E., et al. 2012, PASP, 124, 1000
Stassun, K. G., Oelkers, R. J., Pepper, J., et al. 2018, AJ, 156, 102
Stassun, K. G., Oelkers, R. J., Paegert, M., et al. 2019, AJ, 158, 138
Stumpe, M. C., Smith, J. C., Catanzarite, J. H., et al. 2014, PASP, 126, 100
Stumpe, M. C., Smith, J. C., Van Cleve, J. E., et al. 2012, PASP, 124, 985
Stürmer, J., Seifahrt, A., Schwab, C., & Bean, J. L. 2017, JATIS, 3, 025003
Trifonov, T., Caballero, J. A., Morales, J. C., et al. 2021, Sci, 371, 1038
Twicken, J. D., Catanzarite, J. H., Clarke, B. D., et al. 2018, PASP, 130, 064502
VanderPlas, J. T., & Ivezić, Ž. 2015, ApJ, 812, 18
Vanderspek, R., Huang, C. X., Vanderburg, A., et al. 2019, ApJL, 871, L24
Vogt, S. S., Allen, S. L., Bigelow, B. C., et al. 1994, Proc. SPIE, 2198, 362
Winters, J. G., Charbonneau, D., Henry, T. J., et al. 2021, AJ, 161, 63
Winters, J. G., Medina, A. A., Irwin, J. M., et al. 2019, AJ, 158, 152
Winters, J. G., Irwin, J. M., Charbonneau, D., et al. 2020, AJ, 159, 290
Wood, B. E., Müller, H.-R., Redfield, S., et al. 2021, ApJ, 915, 37
Zechmeister, M., Reiners, A., Amado, P. J., et al. 2018, A&A, 609, A12
Zeng, L., & Sasselov, D. 2013, PASP, 125, 227
Zeng, L., Sasselov, D. D., & Jacobsen, S. B. 2016, ApJ, 819, 127
Zucker, S., & Mazeh, T. 1994, ApJ, 420, 806